The Astrophysical Journal, 1001:213 (21pp), 2026 April 20 https://doi.org/10.3847/1538-4357/ae3a8b
© 2026. The Author(s). Published by the American Astronomical Society.
OPEN ACCESS

Non-Gaussian Expansion of Minkowski Tensors in Redshift Space

Stephen Appleby[1,2], Christophe Pichon[3,4,8], Pravabati Chingangbam[5], Dmitri Pogosyan[6], and Changbom Park[7]
[1] Asia Pacific Center for Theoretical Physics, Pohang 37673, Republic of Korea; stephen.appleby@apctp.org
[2] Department of Physics, POSTECH, Pohang 37673, Republic of Korea
[3] Institut d'Astrophysique de Paris, 98 bis Boulevard Arago, F-75014 Paris, France; pichon@iap.fr
[4] Kyung Hee University, Department of Astronomy & Space Science, Yongin-shi, Gyeonggi-do 17104, Republic of Korea
[5] Indian Institute of Astrophysics, Koramangala II Block, Bangalore 560 034, India; pravabati@gmail.com
[6] Department of Physics, University of Alberta, 11322-89 Avenue, Edmonton, AB T6G 2G7, Canada; pogosyan@ualberta.ca
[7] School of Physics, Korea Institute for Advanced Study, 85 Hoegiro, Dongdaemun-gu, Seoul 02455, Republic of Korea; cbp@kias.re.kr
Received 2025 July 14; revised 2025 December 8; accepted 2026 January 15; published 2026 April 20

Abstract

This paper focuses on extending the use of Minkowski tensors to analyze anisotropic signals in cosmological data, focusing on those introduced by redshift space distortions. We derive the ensemble average of the two translation-invariant, rank-2 Minkowski tensors ($W_1^{0,2}$ and $W_2^{0,2}$) for a matter density field that is perturbatively non-Gaussian in redshift space. This is achieved through the Edgeworth expansion of the joint probability density function of the field and its derivatives, expressing the ensemble averages in terms of cumulants up to cubic order. Our goal is to connect these theoretical predictions to the underlying cosmological parameters, allowing for parameter estimation by measuring them from galaxy surveys. The work builds on previous analyses of Minkowski functionals in both real and redshift space and addresses the effects of Finger-of-God velocity dispersion and shot noise. We validate our predictions by matching them to measurements of the Minkowski tensors from dark matter simulation data, finding that perturbation theory is a qualified success. Nonperturbative Finger-of-God effects remain significant at relatively large scales of $R_G \lesssim 20\,h^{-1}$ Mpc and are particularly pronounced in the components parallel to the line of sight.

Unified Astronomy Thesaurus concepts: Cosmological perturbation theory (341)

1. Introduction

As the Universe evolves, the nonlinear nature of gravitational collapse generates non-Gaussianity in the matter distribution. Non-Gaussianity can be quantified via the N-point functions of cosmological fields, and by extracting these statistics from galaxy data we can better understand structure formation and infer cosmological parameters. A complicating factor in this scenario is that we almost always measure galaxy positions (velocities) in redshift space, which introduces anisotropy along the line of sight due to peculiar motion. The velocities of galaxies is not random; they are infalling into overdensities on all scales. Hence by measuring the distribution of galaxies in redshift space we are simultaneously observing large-scale structure generated by gravitational collapse, and also the infall of galaxies into gravitational potentials generated by the structures. To extract information from anisotropic fields, statistical methodologies can be employed that are specifically designed to capture directional information.

One such example is the Minkowski tensors (MTs), a rank-p generalization of the scalar Minkowski functionals (H. Hadwiger 1957; L. A. Santalo 1976; P. McMullen 1997; S. Alesker 1999; C. Beisbart et al. 2002; D. Hug et al. 2008; G. Schroder-Turk et al. 2010; G. E. Schroder-Turk et al. 2013), which were first introduced to cosmology in C. Beisbart et al. (2001a, 2001b, 2002), P. Chingangbam et al. (2017b), and V. Ganesan & P. Chingangbam (2017). While Minkowski functionals, frequently studied within the context of cosmology (A. L. Melott et al. 1989; J. R. Gott et al. 1990; C. Park & J. R. Gott 1991; C. Park et al. 1992, 2001, 2013; K. R. Mecke et al. 1994; J. Schmalzing & T. Buchert 1997; V. Sahni et al. 1998; J. Schmalzing & K. M. Gorski 1998; S. Bharadwaj et al. 2000; C. Park & Y.-R. Kim 2010; R. van de Weygaert et al. 2011a, 2011b; C. Zunckel et al. 2011; P. Chingangbam & C. Park 2013; N. Shivshankar et al. 2016; P. Chingangbam et al. 2017a; P. Pranav et al. 2017, 2019a, 2019b; S. Rana et al. 2018; J. Feldbrugge et al. 2019; D. Munshi et al. 2021; F. Rahman et al. 2021; G. Wilding et al. 2021; W. Liu et al. 2022, 2023, 2025a), quantify scalar properties (volume, surface area, etc.), MTs quantify directional information, making them ideal for analyzing anisotropic structures found in redshift space (N. Kaiser 1987; W. E. Ballinger et al. 1996; A. J. S. Hamilton 1998; J. L. Tinker 2007; B. A. Reid & M. White 2011; T. Okumura et al. 2012a). The MTs, and closely related statistics (M. H. J. Kanafi & S. M. S. Movahed 2024; A. Afzal et al. 2025), are finding increasing application within cosmology (J. Schmalzing & K. M. Gorski 1998; C. Hikage & T. Matsubara 2012; D. Munshi et al. 2013; A. Kapahtia et al. 2018, 2019, 2021; P. K. Joby et al. 2019; G. A. Marques et al. 2019; S. A. Appleby et al. 2020; P. Goyal et al. 2020; S. Appleby et al. 2021, 2022b; P. Chingangbam et al. 2021; P. Goyal & P. Chingangbam 2021; M. Bashir et al. 2025; W. Liu et al. 2025b). Prior to the introduction of the MTs, it was recognized that the Minkowski functionals extracted from two-dimensional subsets of redshift-

[8] Corresponding author.

Original content from this work may be used under the terms of the Creative Commons Attribution 4.0 licence. Any further this work must maintain attribution to the author(s) and the title of the work, journal citation and DOI.

space data could be used to measure the growth rate f, by varying the angle between the two-dimensional slice and the line of sight (T. Matsubara 1996; S. Codis et al. 2013).

This paper presents a theoretical framework for the MTs extracted from a perturbatively non-Gaussian random field in redshift space. We extend the work of S. Appleby et al. (2018, 2019) to include the leading-order cubic non-Gaussian contribution to the ensemble average of the MTs. This is achieved via the Edgeworth expansion of the joint probability density function (PDF) of the field and its first and second derivatives, and expressing the ensemble averages in terms of cumulants up to cubic order. The work relies on previous analysis performed on the Minkowski functionals in real and redshift space (T. Matsubara 1996, 2003; T. Matsubara & Y. Suto 1996; T. Matsubara & J. Yokoyama 1996; C. Gay et al. 2012; S. Codis et al. 2013), and uses these results to construct the corresponding ensemble averages of the tensors. The ensemble average of the Minkowski functionals of random fields has been extensively studied (A. G. Doroshkevich 1970; R. Adler 1981; J. R. Gott et al. 1986, 1987; J. S. A. Hamilton et al. 1986; H. Tomita 1986; D. H. Weinberg et al. 1987; A. L. Melott et al. 1988; B. S. Ryden et al. 1989; T. Matsubara 1994a, 1994b; C. Hikage et al. 2008; D. Pogosyan et al. 2009; T. Matsubara & S. Kuriki 2021; T. Matsubara et al. 2020; S. Kuriki & T. Matsubara 2023; P. Chingangbam & F. Rahman 2024), but the tensors to a far lesser degree.

Our primary motivation is to express the theoretical predictions for the ensemble averages of the MTs to the underlying cosmological parameters using perturbation theory to describe the two- and three-point cumulants. This connection is useful because it provides a pathway for cosmological parameter estimation by measuring the tensors from observational data. The non-Gaussian components will enhance the constraining power of the statistics by capturing additional information. We also include some complicating factors present in real observations, such as Finger-of-God (FOG) velocity dispersion and shot noise. We validate our theoretical predictions by comparing them to measurements of the MTs obtained from dark matter simulation data. The work serves as a precursor to measuring the MTs from galaxy catalogs, so as to leverage cosmological parameters from the corresponding cumulants.

The rest of the paper will proceed as follows. In Section 2 we briefly introduce the plane-parallel redshift-space distorted field that we will study. In Section 3 we define the MTs that are the main subject of the work, and in Section 4 we construct their ensemble averages in terms of two- and three-point cumulants of the matter density field and its first and second derivatives. In Section 5 we express the cumulants in terms of cosmology using perturbation theory results. In Section 6 we describe the data used in the comparison, and in Section 7 compare the ensemble averages to the numerical extraction of the statistics from dark matter snapshot data. We conclude in Section 8.

2. Redshift-space Fields

In this work, we focus exclusively on plane-parallel redshift-space distorted fields and Cartesian tensors. In S. Appleby et al. (2022a) some of the authors considered the more complicated case of spherical redshift-space distortion, in the Gaussian and Kaiserian limits.

In real space, we assume that the matter density field δ is statistically isotropic and homogeneous. Throughout this work we also assume that the field is mean subtracted. The relation between the real ($\boldsymbol{x}$) and redshift ($\boldsymbol{s}$) space position of a particle is given by

$$\boldsymbol{s} = \boldsymbol{x} + \boldsymbol{e}_3\,(\boldsymbol{v}\cdot\boldsymbol{e}_3)\frac{(1+z)}{H(z)}, \tag{1}$$

where $\boldsymbol{v}$ is the peculiar velocity and $H(z)$ is the Hubble parameter. A more accurate formula would include the effect of the observer peculiar velocity $\boldsymbol{v}_0$ via the replacement $\boldsymbol{v}(\boldsymbol{x}) \to \boldsymbol{v}(\boldsymbol{x}) - \boldsymbol{v}_0$, which accounts for the fact that the effect should decrease for closer objects over scales where peculiar velocities become correlated. In this work we fix $\boldsymbol{v}_0 = 0$, assuming that the observer is sufficiently distant that velocity correlation is negligible.

The plane-parallel approximation has already been implemented via the assumption every tracer particle is subject to a single, parallel line of sight, taken here to be $\boldsymbol{e}_3$. If we now assume a linear relation between the velocity and density field, then the density field in redshift space $\tilde{\delta}$ is related to the real-space field δ according to

$$\tilde{\delta}(\boldsymbol{k}) = (1 + f\mu^2)\,\delta(\boldsymbol{k}), \tag{2}$$

where $\mu = \boldsymbol{k}\cdot\boldsymbol{e}_3/|k|$ is the cosine of the angle between the line of sight and wavenumber $\boldsymbol{k}$, $f = d\ln D/d\ln a$, and D is the linear growth factor. We note that due to the plane-parallel approximation, the field $\tilde{\delta}(\boldsymbol{k})$ is anisotropic but statistically homogeneous. The observed galaxy distribution is radially corrected, and the actual redshift-space field is inhomogeneous due to the presence of a preferred location: the observer at $\boldsymbol{r} = 0$.

The field defined in Equation (2) is the linear density field under the action of the linear Kaiser effect. The expectation value of the MTs measured from such as field has been constructed in S. Appleby et al. (2019). The goal of this work is to calculate the ensemble average of the MTs for fields that are perturbatively non-Gaussian, in redshift space. There are two steps to performing this calculation. First, we use the Edgeworth expansion and the corresponding joint PDF of the redshift-space field and its first and second derivatives, and calculate the ensemble average of the MTs in terms of the cumulants. In this work, we only proceed to the three-point function (bispectrum) contributions, but one could continue to arbitrary order. Second, we write the cumulants in terms of the redshift-space matter power and bispectra. The ultimate goal is to write the ensemble average in terms of cosmological parameters, which will allow us to perform parameter estimation by measuring the MTs from cosmological datasets.

3. Minkowski Tensors: Definitions

The MTs are rank-p generalizations of the scalar Minkowski functionals. To define these statistics, we begin with a smoothed mean zero density field $\delta(\boldsymbol{x})$ with variance $\sigma^2 = \langle\delta^2\rangle$, and define the excursion set at threshold ν as

$$Q(\nu) = \{\boldsymbol{x}|\delta(\boldsymbol{x}) \geqslant \nu\sigma\}.$$

This set contains all spatial regions where the density contrast exceeds the chosen threshold, and its boundary ∂Q is the two-dimensional surface defined by $\delta = \nu\sigma$. For three-dimensional fields, two vectors are associated with an excursion set Q: the position vector $\boldsymbol{x}$ of a point within Q (or on ∂Q), and the unit vector $\hat{\boldsymbol{n}}$ normal to the boundary ∂Q. In this work we focus on rank-2 MTs, which are the lowest-order generalizations of the scalar Minkowski functionals that have nonzero ensemble averages. The complete set of rank-2 tensors that can be constructed from $\boldsymbol{x}$ and $\hat{\boldsymbol{n}}$ is (G. E. Schroder-Turk et al. 2013)

$$W_0^{2,0} = \int_Q \boldsymbol{x}^2 d\mathrm{V}, \tag{3}$$

$$W_k^{r,s} = \int_{\partial Q} G_k \boldsymbol{x}^r \hat{\boldsymbol{n}}^s d\mathrm{A}, \tag{4}$$

where $r + s = 2$, and $\boldsymbol{x}^r = \boldsymbol{x} \otimes \boldsymbol{x}\ldots$ and $\hat{\boldsymbol{n}}^s = \hat{\boldsymbol{n}} \otimes \hat{\boldsymbol{n}}\ldots$ are symmetric tensor products of $\boldsymbol{x}$ and $\hat{\boldsymbol{n}}$, r and s, times, respectively. The factors G_k are $G_1 = 1$, G_2 is the mean curvature of the surface ∂Q, and G_3 is its Gaussian curvature. dV and dA are the volume and area elements, respectively. Of these tensors, we restrict our analysis to the ones that are translation invariant, which are $W_{1,2,3}^{0,2}$ and $W_{1,2,3}^{1,1}$. Between these quantities, linear relations exist of the form (G. E. Schroder-Turk et al. 2013)

$$\mathbb{I}W_k = kW_k^{0,2} + (3 - k)W_{k+1}^{1,1}, \tag{5}$$

where $\mathbb{I}$ is the identity matrix, $k = 0$, 1, 2, and 3, and W_k are the scalar MFs. These relations imply that $W_3^{0,2}$ contains no additional information relative to W_3, and only two of $W_{1,2}^{0,2}$ and $W_{2,3}^{1,1}$ need to be studied beyond the scalar Minkowski functionals. Of these, we focus on

$$W_1^{0,2} = \frac{1}{6V}\int_{\partial Q} \hat{n} \otimes \hat{n}\, dA, \tag{6a}$$

$$W_2^{0,2} = \frac{1}{3\pi V}\int_{\partial Q} \hat{n} \otimes \hat{n}\, G_2 dA. \tag{6b}$$

Note that in the above equations we have normalized by appropriate volume factors, with V being the volume over which the field δ is defined. The mean curvature G_2 can be written as

$$\begin{aligned} G_2 &= -\frac{1}{2}\nabla\cdot\hat{\boldsymbol{n}} = -\frac{1}{2}\left[\frac{\nabla^2\delta}{|\nabla\delta|} - \frac{\nabla\delta}{|\nabla\delta|^2}\cdot\nabla|\nabla\delta|\right] \\ &= -\frac{1}{2|\nabla\delta|^3}\left[(\delta_2^2 + \delta_3^2)\delta_{11} + (\delta_1^2 + \delta_3^2)\delta_{22} + (\delta_1^2 + \delta_2^2)\delta_{33}\right] \\ &\quad + \frac{1}{|\nabla\delta|^3}[\delta_1\delta_2\delta_{12} + \delta_1\delta_3\delta_{13} + \delta_2\delta_3\delta_{23}], \end{aligned} \tag{7}$$

where $\delta_i = \nabla_i\delta$. We can also write the unit normal in terms of derivatives of the field $\hat{n}_i = \delta_i/|\nabla\delta|$. $W_1^{0,2}$ and $W_2^{0,2}$ represent tensorial generalizations of the scalar Minkowski functionals W_1 and W_2, respectively. They describe the surface integrals of the excursion set boundary, now weighted by the product of normals to the surface at each point.

J. Schmalzing & T. Buchert (1997) and J. Schmalzing & K. M. Gorski (1998) have shown how to rewrite the MTs (Equation (6)) as volume integrals:

$$W_1^{0,2}|_i{}^j = \frac{1}{6V}\int dV\delta_{\mathrm{D}}(\delta - \nu\sigma)\frac{\delta_i\delta^j}{|\nabla\delta|}, \tag{8a}$$

$$W_2^{0,2}|_i{}^j = \frac{1}{3\pi V}\int dV\delta_{\mathrm{D}}(\delta - \nu\sigma)\, G_2\frac{\delta_i\delta^j}{|\nabla\delta|}, \tag{8b}$$

where we have introduced $\delta_{\mathrm{D}}(x)$ as the delta function. The $W^{0,2}|_i^j$ are respectively the volume averages of the quantities

$$w_i{}^j \equiv \frac{1}{6}\delta_{\mathrm{D}}(\delta - \nu\sigma)\frac{\delta_i\delta^j}{\sqrt{\delta_k\delta^k}}, \tag{9a}$$

$$v_i{}^j \equiv \frac{1}{3\pi}\delta_{\mathrm{D}}(\delta - \nu\sigma)G_2\frac{\delta_i\delta^j}{\sqrt{\delta_k\delta^k}}\,. \tag{9b}$$

In the following section, we construct the ensemble averages $\langle w_i^j \rangle$ and $\langle v_i^j \rangle$ using the Edgeworth expansion. The former is only a function of the field δ and its first derivatives, whereas the latter is also a function of the second derivatives of the field due to the G_2 term.[9]

4. Ensemble Averages

We start by defining the ensemble averages

$$\langle w_i{}^j \rangle = \int w_i{}^j P(X) dX \,, \quad \langle v_i{}^j \rangle = \int v_i{}^j P(X') dX' \,, \tag{10}$$

where $X = (\delta, \delta_i)$ and $X' = (\delta, \delta_i, \delta_{jk})$ are the set of random variables to which w_i^j and v_i^j are sensitive, and $P(X)$ and $P(X')$ are their joint PDFs. By utilizing linearity of the ensemble average (it is effectively a weighted sum of states) and the assumed statistical homogeneity of the field, the volume and ensemble averages in $\langle W_1^{0,2}|_i{}^j \rangle$ and $\langle W_2^{0,2}|_i{}^j \rangle$ commute, so we can write $\langle w_i{}^j \rangle = \langle W_1^{0,2}|_i{}^j \rangle$ and $\langle v_i{}^j \rangle = \langle W_2^{0,2}|_i{}^j \rangle$. Here we make the implicit assumption that the volume averages constructed from data are representative of the integral over all field configurations which define the ensemble average. In this work we do not study the uncertainty or potential biases that may arise from the finite volume of our simulations; we simply assume ergodicity holds exactly.

The integrals over the random fields can be simplified if the fields exhibit some symmetry. For example, in real space $\delta(\boldsymbol{x})$ is isotropic and we can use $\langle \delta_j \delta_k \rangle \propto \mathbb{I}_{jk}$, where $\mathbb{I}$ is the identity matrix. In redshift space, rotational invariance is partially broken along the line of sight, but the field is assumed to be statistically isotropic in the two-dimensional subspace perpendicular to this direction. We expect the MTs to respect this symmetry, and be of the form $\propto$diag$[a, a, b]$ in a Cartesian coordinate system with bases $\boldsymbol{e}_1$, $\boldsymbol{e}_2$, and $\boldsymbol{e}_3$ that are aligned with the line-of-sight $\boldsymbol{e}_3$. A different choice of coordinates that is not aligned with $\boldsymbol{e}_3$ would generate off-diagonal components. Changes in coordinate systems can be represented by rotation matrices operating on the tensors, and only for an isotropic field are $\langle w_i{}^j \rangle$ and $\langle v_i{}^j \rangle$ diagonal in every coordinate system. Note that we could instead study coordinate invariant quantities such as the eigenvalues of $w_i{}^j$ and $v_i{}^j$, as originally proposed in P. Chingangbam et al. (2017b). However, these are nonlinear functions of the tensor elements and their ensemble averages are not currently known.

4.1. Ensemble Average of $\mathrm{w_i{}^j}$

We follow S. Codis et al. (2013) closely throughout, and so adopt the same variables as that work: $x = \delta/\sigma$, $q_\perp^2 = (\delta_1^2 + \delta_2^2)/\sigma_{1\perp}^2$, and $x_3 = \delta_3/\sigma_{1\parallel}$. The cumulants σ^2, $\sigma_{1\parallel}^2$, and $\sigma_{1\perp}^2$ are the field variances for δ, δ_3, and $\sqrt{\delta_1^2 + \delta_2^2}$, respectively. The joint PDF $P(x, q_\perp^2, x_3)$, up to cubic order in the cumulants, is given by

$$P(x, q_\perp^2, x_3) = \frac{1}{2\pi} e^{-x^2/2 - q_\perp^2 - x_3^2/2} \left[1 + \sum_{\kappa_3} \frac{(-1)^j}{i!j!k!} \langle x^i q_\perp^{2j} x_3^k \rangle \, H_i(x) L_j(q_\perp^2) H_k(x_3) \right], \tag{11}$$

where the sum over $\kappa_3 = \{i + 2j + k = 3\}$ is over all combinations of integers i, $2j$, and $k \geqslant 0$ that sum to 3. $H_i(x)$ and $L_k(x)$ are probabilist Hermite and Laguerre polynomials, respectively.[10]

Using these dimensionless variables, the MT can be written as

$$w_1{}^1 + w_2{}^2 = \frac{\sigma_{1\perp}}{6\sigma} \delta_{\mathrm{D}}(x - \nu) \frac{q_\perp^2}{\tilde{X}}, \tag{12a}$$

$$w_3{}^3 = \frac{\sigma_{1\perp} \lambda^2}{6\sigma} \delta_{\mathrm{D}}(x - \nu) \frac{x_3^2}{\tilde{X}}, \tag{12b}$$

where $\tilde{X} = \sqrt{q_\perp^2 + \lambda^2 x_3^2}$ and $\lambda = \sigma_{1\parallel}/\sigma_{1\perp}$. All off-diagonal terms will be zero in this coordinate system. The ensemble average of the nonzero components of $w_i{}^j$ is then given by

$$\langle w_1{}^1 \rangle + \langle w_2{}^2 \rangle = \frac{\sigma_{1\perp}}{6\sigma} \int dq_\perp^2 dx_3 P(\nu, q_\perp^2, x_3) \frac{q_\perp^2}{\tilde{X}} \,, \tag{13a}$$

$$\langle w_3{}^3 \rangle = \frac{\sigma_{1\perp}}{6\sigma} \int dq_\perp^2 dx_3 P(\nu, q_\perp^2, x_3) \frac{\lambda^2 x_3^2}{\tilde{X}} \,, \tag{13b}$$

[9] In this work we focus on calculating the components of the tensors in a particular coordinate system, and we direct the reader to T. Matsubara (2024a, 2024b, 2024c, 2024d) for a more general formalism for extracting information from tensors.

[10] The first few of which are $H_0 = 1$, $H_1 = x$, $H_2 = x^2 - 1$, and $H_3 = x^3 - 3x$, and $L_0 = 1$, $L_2 = 1 - x$, and $L_3 = (x^2 - 4x + 2)/2$.

where the integrals are over $x_3 \in (-\infty, \infty)$ and $q_\perp^2 \in [0, \infty)$. Integrating over the gradients $q_\perp^2$ and x_3 using `Mathematica`, we find

$$\langle w_1{}^1\rangle + \langle w_2{}^2\rangle = \frac{\sigma_{1\perp} e^{-\nu^2/2}}{6\pi\sigma}\left[A_{\mathrm{G}\perp}^{(1)}\left(H_0(\nu) + \frac{\langle x^3\rangle}{6}H_3(\nu)\right) + (B_\perp^{(1)}\langle x q_\perp^2\rangle + C_\perp^{(1)}\langle x x_3^2\rangle) H_1(\nu) + \mathcal{O}(\sigma^2)\right], \tag{14a}$$

$$\langle w_3{}^3\rangle = \frac{\sigma_{1\perp} e^{-\nu^2/2}}{6\pi\sigma}\left[A_{\mathrm{G}\parallel}^{(1)}\left(H_0(\nu) + \frac{\langle x^3\rangle}{6}H_3(\nu)\right) + (B_\parallel^{(1)}\langle x q_\perp^2\rangle + C_\parallel^{(1)}\langle x x_3^2\rangle)H_1(\nu) + \mathcal{O}(\sigma^2)\right], \tag{14b}$$

where the coefficients depend on λ and are given by

$$A_{\mathrm{G}\perp}^{(1)} = \frac{\sqrt{2}\,(4\lambda^2-1)}{4(2\lambda^2-1)^{3/2}}\cosh^{-1}(4\lambda^2-1) - \frac{\lambda}{2\lambda^2-1}, \tag{15a}$$

$$B_\perp^{(1)} = \frac{\lambda(10\lambda^2-16\lambda^4-1)}{2(2\lambda^2-1)^3} + \frac{16\lambda^4-4\lambda^2+1}{4\sqrt{2}\,(2\lambda^2-1)^{5/2}}\cosh^{-1}(4\lambda^2-1), \tag{15b}$$

$$C_\perp^{(1)} = \frac{3\lambda^3}{(2\lambda^2-1)^2} - \frac{\sqrt{2}\,(8\lambda^2-1)}{4(2\lambda^2-1)^{5/2}}\cosh^{-1}(\sqrt{2}\,\lambda)\,\frac{\sqrt{2}\,(4\lambda^2-1)}{8(2\lambda^2-1)^{3/2}}\cosh^{-1}(4\lambda^2-1), \tag{15c}$$

$$A_{\mathrm{G}\parallel}^{(1)} = \frac{2\lambda^3}{2\lambda^2-1} - \frac{\sqrt{2}\,\lambda^2}{(2\lambda^2-1)^{3/2}}\cosh^{-1}(\sqrt{2}\,\lambda), \tag{15d}$$

$$B_\parallel^{(1)} = \frac{3\lambda^3}{(2\lambda^2-1)^2} - \frac{\lambda^2(1+4\lambda^2)}{\sqrt{2}\,(2\lambda^2-1)^{5/2}}\cosh^{-1}(\sqrt{2}\,\lambda), \tag{15e}$$

$$C_\parallel^{(1)} = \frac{2\lambda^3(2\lambda^4-5\lambda^2+2)}{(2\lambda^2-1)^3} + \frac{\sqrt{2}\,\lambda^2(1+\lambda^2)}{2(2\lambda^2-1)^{5/2}}\cosh^{-1}(4\lambda^2-1). \tag{15f}$$

The Gaussian limit of the ensemble average is

$$\langle w_1{}^1\rangle_{\mathrm{G}} + \langle w_2{}^2\rangle_{\mathrm{G}} = \frac{\sigma_{1\perp} e^{-\nu^2/2}}{6\pi\sigma} A_{\mathrm{G}\perp}^{(1)} H_0(\nu), \tag{16a}$$

$$\langle w_3{}^3\rangle_{\mathrm{G}} = \frac{\sigma_{1\perp} e^{-\nu^2/2}}{6\pi\sigma} A_{\mathrm{G}\parallel}^{(1)} H_0(\nu). \tag{16b}$$

The trace of the ensemble averages in Equations (16) and (14) should respectively yield the expectation value of the scalar Minkowski functional W_1 in redshift space for a Gaussian, Kaiser-corrected field and the leading-order non-Gaussian result derived in T. Matsubara (1996) and S. Codis et al. (2013). We have verified numerically that our results agree with the previous literature, in particular we present a comparison between our results and those of S. Codis et al. (2013) in Appendix A (see Figure 6).

4.2. Ensemble Average of $\mathrm{v_i}^{\mathrm{j}}$

The ensemble average of ${v_i}^j$ proceeds similarly to ${w_i}^j$, but with some complicating factors. We again define everything in terms of the dimensionless variables introduced in S. Codis et al. (2013). In addition to x, $q_\perp^2$, and x_3 used in the previous section, we introduce the terms $x_1 = \delta_1/\sigma_{1\perp}$, $x_2 = \delta_2/\sigma_{1\perp}$, $J_{1\perp} = (\delta_{11}+\delta_{22})/\sigma_{2\perp}$, $x_{11} = \delta_{11}/\sigma_{2\perp}$, $x_{22} = \delta_{22}/\sigma_{2\perp}$, $x_{33} = \delta_{33}/\sigma_{2\parallel}$, $x_{12} = \delta_{12}/\sigma_{2\perp}$, $x_{13} = \delta_{13}/\sigma_Q^2$, and $x_{23} = \delta_{23}/\sigma_Q^2$. These quantities have variances

$$\langle x_1^2\rangle = \langle x_2^2\rangle = \frac{1}{2}\,, \quad \langle J_{1\perp}^2\rangle = 1\,,\ \langle x_{11}^2\rangle = \langle x_{22}^2\rangle = \frac{3}{8}\,, \quad \langle x_3^2\rangle = 1\,,\ \langle x_{12}^2\rangle = \frac{1}{8}\,, \quad \langle x_{13}^2\rangle = \langle x_{23}^2\rangle = \frac{1}{2}. \tag{17}$$

In terms of these variables, we have

$$v_1{}^1 + v_2{}^2 = \frac{\sigma_{1\perp}}{3\pi\sigma}\delta_{\mathrm{D}}(x-\nu)G_2\frac{q_\perp^2}{\tilde{X}}, \tag{18a}$$

$$v_3{}^3 = \frac{\sigma_{1\perp}\lambda^2}{3\pi\sigma}\delta_{\mathrm{D}}(x-\nu)G_2\frac{x_3^2}{\tilde{X}}, \tag{18b}$$

with

$$G_2 = -\frac{1}{2\sigma_{1\perp}\tilde{X}^3}\left[(x_2^2 + \lambda^2 x_3^2)\sigma_{2\perp}x_{11} + (x_1^2 + \lambda^2 x_3^2)\sigma_{2\perp}x_{22} + \sigma_{2\parallel}q_\perp^2 x_{33}\right] + \frac{1}{\sigma_{1\perp}\tilde{X}^3}\left[\sigma_{2\perp}x_1x_2x_{12} + \lambda\sigma_Q x_1x_3x_{13} + \lambda\sigma_Q x_2x_3x_{23}\right]. \tag{19a}$$

We note that there are six terms in G_2, and each contains a single second derivative. We can calculate the ensemble average of each separately. The terms proportional to x_{11}, x_{22}, and x_{33} must be decorrelated from x using the new variables

$$y_{11} = \frac{x_{11} + \gamma_\perp x}{\sqrt{1-\gamma_\perp^2}},\ y_{22} = \frac{x_{22} + \gamma_\perp x}{\sqrt{1-\gamma_\perp^2}},\ y_{33} = \frac{x_{33} + \gamma_\parallel x}{\sqrt{1-\gamma_\parallel^2}}, \tag{20}$$

where $\gamma_\perp = \sigma_{1\perp}^2/(\sigma\sigma_{2\perp})$ and $\gamma_\parallel = \sigma_{1\parallel}^2/(\sigma\sigma_{2\parallel})$. We do not need to decorrelate the second derivatives from one another using the more complicated transformation used in S. Codis et al. (2013), because all second derivatives appear linearly in ${v_i}^j$, meaning that all components except one can be marginalized out for each term in G_2. Finally, each of the six contributions to $\langle {v_i}^j\rangle$ can be integrated over the joint probability $P(x, x_1, x_2, x_3, \kappa)$, where $\kappa = (x_{11}, x_{22}, x_{33}, x_{12}, x_{13}, x_{23})$ depending on the term being calculated. The final integrals can be transformed from (x_1, x_2, x_3) to $(q_\perp^2, x_3)$ using the symmetry of the field, and we can use $\langle x_i^2 x_{ii}\rangle = 0$ and $\langle x_1^2 x_{33}\rangle/\gamma_\parallel = \langle x_3^2 x_{11}\rangle/\gamma_\perp$ to simplify the final result. After a tedious calculation, we can write the ensemble averages purely in terms of the variables defined in S. Codis et al. (2013) as

$$\langle {v_1}^1\rangle + \langle {v_2}^2\rangle = \frac{\sigma_{1\perp}^2}{12\pi\sqrt{2\pi}\,\sigma^2}e^{-\nu^2/2}\left[A_{G\perp}^{(2)}\left(H_1(\nu) + \frac{\langle x^3\rangle}{6}H_4(\nu)\right) + (B_\perp^{(2)}\langle xq_\perp^2\rangle + C_\perp^{(2)}\langle xx_3^2\rangle)H_2(\nu) + \left(D_\perp^{(2)}\frac{\langle q_\perp^2 J_{1\perp}\rangle}{\gamma_\perp} + E_\perp^{(2)}\frac{\langle x_3^2 J_{1\perp}\rangle}{\gamma_\perp}\right)H_0(\nu) + \mathcal{O}(\sigma^2)\right], \tag{21a}$$

$$\langle {v_3}^3\rangle = \frac{\sigma_{1\perp}^2}{12\pi\sqrt{2\pi}\,\sigma^2}e^{-\nu^2/2}\left[A_{G\parallel}^{(2)}\left(H_1(\nu) + \frac{\langle x^3\rangle}{6}H_4(\nu)\right) + (B_\parallel^{(2)}\langle xq_\perp^2\rangle + C_\parallel^{(2)}\langle xx_3^2\rangle)H_2(\nu) + \left(D_\parallel^{(2)}\frac{\langle q_\perp^2 J_{1\perp}\rangle}{\gamma_\perp} + E_\parallel^{(2)}\frac{\langle x_3^2 J_{1\perp}\rangle}{\gamma_\perp}\right)H_0(\nu) + \mathcal{O}(\sigma^2)\right], \tag{21b}$$

where

$$A_{G\perp}^{(2)} = \frac{2\lambda^4 - 3\lambda^2 + 1 + 2\lambda^4\sqrt{2\lambda^2-1}\tan^{-1}\sqrt{2\lambda^2-1}}{(2\lambda^2-1)^2}, \tag{22a}$$

$$B_\perp^{(2)} = \frac{2\lambda^6 - 9\lambda^4 + 6\lambda^2 - 1 + 2\lambda^4(1+\lambda^2)\sqrt{2\lambda^2-1}\tan^{-1}\sqrt{2\lambda^2-1}}{(2\lambda^2-1)^3}, \tag{22b}$$

$$C_\perp^{(2)} = \frac{2\lambda^6 + \lambda^4 - \lambda^2 + 2\lambda^4(\lambda^2-2)\sqrt{2\lambda^2-1}\tan^{-1}\sqrt{2\lambda^2-1}}{(2\lambda^2-1)^3}, \tag{22c}$$

$$D_\perp^{(2)} = \frac{10\lambda^4 - 7\lambda^2 + 1 - 6\lambda^4\sqrt{2\lambda^2-1}\tan^{-1}\sqrt{2\lambda^2-1}}{(2\lambda^2-1)^3}, \tag{22d}$$

$$E_\perp^{(2)} = \frac{-2\lambda^6 - \lambda^4 + \lambda^2 - 2\lambda^4(\lambda^2-2)\sqrt{2\lambda^2-1}\tan^{-1}\sqrt{2\lambda^2-1}}{(2\lambda^2-1)^3}, \tag{22e}$$

$$A_{G\parallel}^{(2)} = \frac{2\lambda^4 - \lambda^2 + 2\lambda^2(\lambda^2-1)\sqrt{2\lambda^2-1}\tan^{-1}\sqrt{2\lambda^2-1}}{(2\lambda^2-1)^2}, \tag{22f}$$

$$B_\parallel^{(2)} = \frac{2\lambda^6 + \lambda^4 - \lambda^2 + 2\lambda^4(\lambda^2-2)\sqrt{2\lambda^2-1}\tan^{-1}\sqrt{2\lambda^2-1}}{(2\lambda^2-1)^3}, \tag{22g}$$

$$C_{\parallel}^{(2)} = \frac{2\lambda^6 - 5\lambda^4 + 2\lambda^2 + 2(\lambda^6 - \lambda^4 + \lambda^2)\sqrt{2\lambda^2 - 1}\tan^{-1}\sqrt{2\lambda^2 - 1}}{(2\lambda^2 - 1)^3}, \tag{22h}$$

$$D_{\parallel}^{(2)} = \frac{-6\lambda^4 + 3\lambda^2 + 2\lambda^2(\lambda^2 + 1)\sqrt{2\lambda^2 - 1}\tan^{-1}\sqrt{2\lambda^2 - 1}}{(\lambda^2 - 1)^3}, \tag{22i}$$

$$E_{\parallel}^{(2)} = \frac{-2\lambda^6 + 5\lambda^4 - 2\lambda^2 - 2\lambda^2(\lambda^4 - \lambda^2 + 1)\sqrt{2\lambda^2 - 1}\tan^{-1}\sqrt{2\lambda^2 - 1}}{(2\lambda^2 - 1)^3}, \tag{22j}$$

recalling that the anisotropy is encoded in $\lambda = \sigma_{1\parallel}/\sigma_{1\perp}$. The trace of this statistic yields the Minkowski functional W_2 in redshift space.

The Gaussian and Kaiserian limits of the ensemble averages are

$$\langle \nu_1{}^1\rangle_{\rm G} + \langle \nu_2{}^2\rangle_{\rm G} = \frac{\sigma_{1\perp}^2}{12\pi\sqrt{2\pi}\,\sigma^2} e^{-\nu^2/2} A_{{\rm G}\perp}^{(2)} H_1(\nu), \tag{23a}$$

$$\langle \nu_3{}^3\rangle_{\rm G} = \frac{\sigma_{1\perp}^2}{12\pi\sqrt{2\pi}\,\sigma^2} e^{-\nu^2/2} A_{{\rm G}\parallel}^{(2)} H_1(\nu). \tag{23b}$$

We have checked that Equation (23) agrees with previous calculations in redshift space (S. Appleby et al. 2019). The trace of Equation (21) should yield the Minkowski functional W_2, however the non-Gaussian form of W_2 was not derived in S. Codis et al. (2013). To our knowledge, Equation (21) represents the first derivation of W_2 to leading non-Gaussian order in redshift space. In Appendix A we show that in the isotropic limit, the trace of Equation (21) coincides with W_2 calculated in T. Matsubara (2003).

To make use of Equations (14) and (21) we must express the cosmological dependence of the cumulants σ, $\sigma_{1\parallel}$, $\sigma_{1\perp}$, λ, $\langle x^3\rangle$, $\langle x q_\perp^2\rangle$, $\langle x x_3^2\rangle$, $\langle q_\perp^2 J_{1\perp}\rangle$, and $\langle x_3^2 J_{1\perp}\rangle$. This will be the subject of Section 5. Note importantly that all third-order cumulants in Equations (14) and (21) are linearly sensitive to the amplitude of matter fluctuations σ, so measuring the non-Gaussian contribution to the MT curves gives us access to both the growth rate $f\sigma_8$ and the amplitude $b_1\sigma_8$.

5. Cumulants in Redshift Space

As the next step, we need to express the two- and three-point cumulants as functions of the cosmological parameters. Fortunately, this has already been done in S. Codis et al. (2013) for the purpose of calculating the scalar Minkowski functionals in redshift space; in real space the cumulants up to the trispectrum were constructed in T. Matsubara et al. (2020). In this section we review the work of S. Codis et al. (2013).

We note that the variables used in this work differ from those in S. Appleby et al. (2019, 2022a), where the ensemble expectation values of the MTs in the Gaussian limit were constructed. In those works, the authors used cumulants that asymptote to their isotropic limits as $f \to 0$. In contrast, here we use precisely the definitions of S. Codis et al. (2013), to avoid confusion. We have checked that mapping the conventions in this work yields the same Gaussian limit as in S. Appleby et al. (2019, 2022a).

5.1. Two-point Cumulants

The two-point cumulants in redshift space are given by

$$\sigma^2 = \frac{1}{(2\pi)^2}\int_{-1}^{1} d\mu \int_0^\infty dk\, k^2 (1 + f\mu^2)^2 P_m(k, z) W^2(kR_{\rm G}), \tag{24a}$$

$$\sigma_{1\parallel}^2 = \frac{1}{(2\pi)^2}\int_{-1}^{1} d\mu \int_0^\infty dk\, k^4 \mu^2 (1 + f\mu^2)^2 P_m(k, z) W^2(kR_{\rm G}), \tag{24b}$$

$$\sigma_{1\perp}^2 = \frac{1}{(2\pi)^2}\int_{-1}^{1} d\mu \int_0^\infty dk\, k^4 (1 - \mu^2)(1 + f\mu^2)^2 P_m(k, z) W^2(kR_{\rm G}), \tag{24c}$$

$$\sigma_{2\parallel}^2 = \frac{1}{(2\pi)^2}\int_{-1}^{1} d\mu \int_0^\infty dk\, k^6 \mu^4 (1 + f\mu^2)^2 P_m(k, z) W^2(kR_{\rm G}), \tag{24d}$$

$$\sigma_{2\perp}^2 = \frac{1}{(2\pi)^2}\int_{-1}^{1} d\mu \int_0^\infty dk\, k^6 (1 - \mu^2)^2 (1 + f\mu^2)^2 P_m(k, z) W^2(kR_{\rm G}), \tag{24e}$$

$$\sigma_Q^2 = \frac{1}{(2\pi)^2}\int_{-1}^{1} d\mu \int_0^\infty dk\, k^6 \mu^2 (1 - \mu^2)(1 + f\mu^2)^2 P_m(k, z) W^2(kR_{\rm G}), \tag{24f}$$

where we have introduced the isotropic, linear matter power spectrum $P_m(k, z)$ evaluated at redshift z, and smoothing kernel $W(kR_{\rm G}) = e^{-k^2 R_{\rm G}^2/2}$ for some comoving smoothing scale $R_{\rm G}$. The μ integrals can be performed analytically, but in what follows we will introduce an additional μ-dependent kernel to account for the FOG effect. We use CAMB[11] to estimate $P_m(k, z)$ for a given

Table 1
Bispectrum Kernels for Each of the Cumulants Pertinent to $\langle w_i{}^j \rangle$ and $\langle v_i{}^j \rangle$

$\mathcal{Y}$	$\alpha(\boldsymbol{k}_1, \boldsymbol{k}_2)$	$\beta(\boldsymbol{k}_1, \boldsymbol{k}_2)$
x^3	$3/\sigma^3$	$3/\sigma^3$
$xq_\perp^2$	$k_{1\perp}^2/(\sigma\sigma_{1\perp}^2)$	$[\boldsymbol{k}_{1\perp}.\boldsymbol{k}_{2\perp} + 2k_{1\perp}^2]/(\sigma\sigma_{1\perp}^2)$
xx_3^2	$k_{1\parallel}^2/(\sigma\sigma_{1\parallel}^2)$	$[k_{1\parallel}k_{2\parallel} + 2k_{1\parallel}^2]/(\sigma\sigma_{1\parallel}^2)$
$q_\perp^2 J_{1\perp}$	0	$[(\boldsymbol{k}_{1\perp}.\boldsymbol{k}_{2\perp})^2 - (\boldsymbol{k}_{1\perp} \times \boldsymbol{k}_{2\perp})^2 - k_{1\perp}^2 k_{2\perp}^2]/(\sigma_{1\perp}^2\sigma_{2\perp})$
$x_3^2 J_{1\perp}$	0	$[k_{1\parallel}k_{2\parallel}(\boldsymbol{k}_{1\perp} + \boldsymbol{k}_{2\perp})^2 - 2k_{1\perp}^2 k_{2\parallel}(k_{1\parallel} + k_{2\parallel})]/(\sigma_{1\parallel}^2\sigma_{2\perp})$

cosmology and define the ith isotropic cumulant as

$$\sigma_i^2 = \frac{1}{2\pi^2}\int_0^\infty dk k^{2i+2} P_m(k, z) W^2(kR_{\rm G}). \tag{25}$$

5.2. Three-point Cumulants

The statistic $\langle w_i{}^j \rangle$ is sensitive to the cubic cumulants $\langle x^3 \rangle$, $\langle xx_I^2 \rangle$, and $\langle xx_3^2 \rangle$. The second MT $\langle v_i{}^j \rangle$ is also sensitive to $\langle q_\perp^2 J_{1\perp} \rangle$ and $\langle x_3^2 J_{1\perp} \rangle$. By utilizing isotropy in the plane perpendicular to the line of sight, the cumulants $\langle xx_I x_3 \rangle$ and $\langle xx_I x_J \rangle$, $I \neq J$ are zero.

For a dark matter field, the nonzero cumulants are given by S. Codis et al. (2013); they generically obey

$$\langle \mathcal{Y} \rangle = \int \frac{d^3k_1}{(2\pi)^3}\frac{d^3k_2}{(2\pi)^3}\left(\frac{b_2}{2}Z_1^2(\boldsymbol{k}_1)P_m(k_1, z)P_m(k_2, z)\alpha(\boldsymbol{k}_1, \boldsymbol{k}_2) + 2Z_1(\boldsymbol{k}_1)Z_1(\boldsymbol{k}_2)Z_2(\boldsymbol{k}_1, \boldsymbol{k}_2)P_m(k_1, z)P_m(k_2, z)\beta(\boldsymbol{k}_1, \boldsymbol{k}_2)\right), \tag{26}$$

where $\mathcal{Y} = x^3$, $xq_\perp^2$, xx_3^2, $q_\perp^2 J_{1\perp}$, and $x_3^2 J_{1\perp}$. The functions $\beta(\boldsymbol{k}_1, \boldsymbol{k}_2)$ for each $\mathcal{Y}$ are given in Table 1, while the redshift-space kernels Z_1 and Z_2 are

$$Z_1(\boldsymbol{k}_i) = b_1 + f\mu_i^2, \tag{27a}$$

$$Z_2(\boldsymbol{k}_i, \boldsymbol{k}_j) = b_1 F_2(\boldsymbol{k}_i, \boldsymbol{k}_j) + \frac{b_2}{2} + f\mu_{ij}^2 G_2(\boldsymbol{k}_i, \boldsymbol{k}_j) + \frac{f\mu_{ij}k_{ij}}{2}b_1\left(\frac{\mu_i}{k_i} + \frac{\mu_j}{k_j}\right) + \frac{(f\mu_{ij}k_{ij})^2}{2}\frac{\mu_i}{k_i}\frac{\mu_j}{k_j}, \tag{27b}$$

$$F_2(\boldsymbol{k}_i, \boldsymbol{k}_j) = \frac{5}{7} + \frac{m_{ij}}{2}\left(\frac{k_i}{k_j} + \frac{k_j}{k_i}\right) + \frac{2}{7}m_{ij}^2, \tag{27c}$$

$$G_2(\boldsymbol{k}_i, \boldsymbol{k}_j) = \frac{3}{7} + \frac{m_{ij}}{2}\left(\frac{k_i}{k_j} + \frac{k_j}{k_i}\right) + \frac{4}{7}m_{ij}^2, \tag{27d}$$

where $m_{ij} = \boldsymbol{k}_i \cdot \boldsymbol{k}_j/(k_i k_j)$, $\boldsymbol{k}_{ij} = \boldsymbol{k}_i + \mathbf{k}_j$, $\mu_{ij} = \boldsymbol{k}_{ij} \cdot \boldsymbol{e}_3/k_{ij} = (\mu_i k_i + \mu_j k_j)/k_{ij}$, and $\mu_i = \boldsymbol{k}_i \cdot \boldsymbol{e}_3/k_i$. Although we focus on dark matter in this work, we include b_1 and b_2 in the cumulants, which are, respectively, the first- and second-order bias parameters and will be pertinent to galaxy data in the future. In what follows we fix $b_1 = 1$ and $b_2 = 0$.

To proceed with integration of Equation (26) in redshift space we decompose the Fourier modes into vectors projected perpendicular and parallel to the line of sight: $\boldsymbol{k} = \boldsymbol{k}_\parallel + \boldsymbol{k}_\perp$ with $\boldsymbol{k}_\perp \cdot \boldsymbol{e}_3 = 0$, $\boldsymbol{k}_\parallel \cdot \boldsymbol{e}_3 = k_\parallel$, $\boldsymbol{k}_\parallel \cdot \boldsymbol{k}_\perp = 0$, and θ_{12}, the angle between $\boldsymbol{k}_{1\perp}$ and $\boldsymbol{k}_{2\perp}$ in the plane perpendicular to $\boldsymbol{e}_3$. In terms of the magnitudes and angles defined above, we can write $k_{i,\parallel} = \mu_i k_i$, $k_{i,\perp} = \sqrt{1-\mu_i^2}k_i$, $\boldsymbol{k}_{i,\perp} \cdot \boldsymbol{k}_{j,\perp} = \sqrt{1-\mu_i^2}\sqrt{1-\mu_j^2}k_i k_j \cos\theta_{ij}$ and

$$k_i = \sqrt{k_{i,\parallel}^2 + k_{i,\perp}^2}, \quad \mu_i = k_{i,\parallel}/k_i, \tag{28a}$$

$$k_{ij} = \sqrt{k_{i,\parallel}^2 + k_{i,\perp}^2 + k_{j,\parallel}^2 + k_{j,\perp}^2 + 2k_{i,\parallel}k_{j,\parallel} + 2\boldsymbol{k}_{i,\perp} \cdot \boldsymbol{k}_{j,\perp}}, \tag{28b}$$

$$\mu_{ij} = (k_{i,\parallel} + k_{j,\parallel})/k_{ij}, \quad m_{ij} = (k_{i,\parallel}k_{j,\parallel} + \boldsymbol{k}_{i,\perp} \cdot \boldsymbol{k}_{j,\perp})/(k_i k_j). \tag{28c}$$

In redshift space, five of the six Fourier mode integrations are nontrivial. There is a single trivial integration, which is one of the angles in the plane perpendicular to the line of sight. Specifically, only the relative angle between $\boldsymbol{k}_{i,\perp}$ and $\boldsymbol{k}_{j,\perp}$ enters into the bispectrum kernels, because the field is isotropic in this plane. Thus, with the inclusion of the smoothing kernels, we can present the

[11] https://github.com/cmbant/CAMB

Fourier integrals as follows:

$$\int \frac{d^3k_1}{(2\pi)^3}\frac{d^3k_2}{(2\pi)^3} \to \frac{1}{(2\pi)^5}\int k_1^2 k_2^2 dk_1 dk_2 d\mu_1 d\mu_2 d\theta_{12} W_G(k_1R_G) W_G(k_2R_G) W_G(|\boldsymbol{k}_1 + \boldsymbol{k}_2|R_G),$$

5.3. Finger-of-God Effect

Beyond the perturbative non-Gaussianity generated by gravitational collapse, there is an additional effect due to stochastic velocities of bound systems scattering the redshift-space positions of tracer particles along the line of sight. This FOG velocity dispersion can be significant even on relatively large scales (R. Juszkiewicz et al. 1998; C. Hikage & K. Yamamoto 2013; F. Beutler et al. 2014; B. A. Reid et al. 2014; T. Okumura et al. 2015; M. Tonegawa et al. 2020); this was also observed in S. Appleby et al. (2022a). To account for the effect, we introduce an additional μ-dependent function in the two- and three-point cumulant definitions (P. J. E. Peebles 1976; C. Park et al. 1994; J. A. Peacock & S. J. Dodds 1994; R. Scoccimarro 2004; V. Desjacques & R. K. Sheth 2010). Specifically, the smoothing kernel in the two-point cumulants (Equation (24)) is modified to

$$W^2(kR_G) \to W^2(kR_G)e^{-k^2\mu^2\sigma_v^2}, \tag{29}$$

and the three-point cumulant integrand (Equation (26)) is modified to (remembering that we are fixing $b_2 = 0$)

$$2[Z_2(\boldsymbol{k}_1, \boldsymbol{k}_2)Z_1(\boldsymbol{k}_1)Z_1(\boldsymbol{k}_2)P_m(k_1, z)P_m(k_2, z)e^{-(k_1^2\mu_1^2+k_2^2\mu_2^2)\sigma_B^2}], \tag{30}$$

with two free parameters, σ_v and σ_B. This is a phenomenological parameterization, and as we will see the presence of stochastic velocity dispersion disproportionately affects the components of $\langle w_i{}^j\rangle$ and $\langle v_i{}^j\rangle$ parallel to the line of sight. Due to the phenomenological nature of the prescription, the parameters σ_v and σ_B are sometimes treated as independent parameters to be jointly constrained. In this work we always fix them to be equal.

5.4. Shot Noise

We can add shot noise to the two-point cumulants by modifying the matter power spectrum according to $P_m(k, z) \to P_m(k, z) + \bar{n}^{-1}$, where $\bar{n}$ is the number density of the point distribution. Similarly, we can add shot noise to the bispectrum. Specifically the integrand defined in Equation (30) picks up an additive correction of the form (S. Matarrese et al. 1997)

$$B_{\rm shot}(k_1, k_2, |\boldsymbol{k}_1 + \boldsymbol{k}_2|, z) = \epsilon_0 + \eta_0[P_m(k_1, z) + P_m(k_2, z) + P_m(|\boldsymbol{k}_1 + \boldsymbol{k}_2|, z)]. \tag{31}$$

If we assume that the shot noise is Poissonian, then $\epsilon_0 = 1/\bar{n}^2$ and $\eta_0 = 1/\bar{n}$, and $P_m(k, z)$ is the power spectrum without any shot noise included. However, in this work we focus on dark matter and smooth on scales much larger than the mean particle separation, meaning that shot noise will be completely suppressed. Practically, when $\bar{n}^{-1/3} \ll R_G$ these contributions can be neglected.

6. Data and Methodology

To confirm the results derived in the previous section, we compare $\langle w_i{}^j\rangle$ and $\langle v_i{}^j\rangle$ to numerical reconstructions of $W_1^{0,2}$ and $W_2^{0,2}$. In this section we review the mock data and numerical algorithms used to estimate $W_1^{0,2}$ and $W_2^{0,2}$. We direct the reader to G. Schroder-Turk et al. (2010), G. E. Schroder-Turk et al. (2013), and C. Collischon et al. (2024) for related numerical studies of the MTs.

To study redshift-space MTs of the non-Gaussian dark matter density field in simulations, we use $N_{\rm real} = 100$ number of realizations of $z = 1$ snapshot boxes from the Quijote simulations (F. Villaescusa-Navarro et al. 2020). These are a suite of dark matter simulations in which ∼44,000 realizations of 512^3 particles are gravitationally evolved in boxes of size $L = 1000\,h^{-1}$ Mpc from $z = 127$ to $z = 0$. We use data from the fiducial cosmology, with parameters $[\Omega_m, \Omega_b, h, n_s, \sigma_8] = [0.3175, 0.049, 0.6711, 0.9624, 0.834]$.

To generate the plane-parallel redshift-space distorted fields, we define the redshift-space positions of the dark matter particles ($\boldsymbol{s}$) by perturbing their real-space positions ($\boldsymbol{x}$) according to

$$\boldsymbol{s} = \boldsymbol{x} + \boldsymbol{e}_3(\boldsymbol{v}\cdot\boldsymbol{e}_3)\frac{(1+z)}{H(z)}, \tag{32}$$

where $\boldsymbol{v}$ is the velocity of the particle, $\boldsymbol{e}_3$ is the unit vector aligned with the x_3 direction of the Cartesian grid that is taken to be the line of sight, and we take $z = 1$. Periodicity is enforced after the redshift-space correction. There are two reasons why we make our measurements at $z = 1$. First, perturbation theory is applicable on relatively smaller scales at higher redshift. Second, modern datasets typically observe galaxies at $z \sim 1$, making this regime more pertinent than $z = 0$ data.

After moving the dark matter particles to their redshift-space position, we bin them into pixels using a cloud-in-cell scheme, using a regular Cartesian lattice with $N = 256$ pixels per side of resolution $\Delta = 1000/256 = 3.9\,h^{-1}$ Mpc and define the number density field $\delta_{ijk} = (n_{ijk} - \bar{n})/\bar{n}$. We smooth these fields with Gaussian kernel $W(kR_G) = e^{-k^2R_G^2/2}$ in Fourier space, calculate the mean $\bar{\delta}$ and variance σ^2 after smoothing, and finally construct the zero mean, unit variance density field $\delta_{ijk} \to (\delta_{ijk} - \bar{\delta})/\sigma$. The quantities $W_1^{0,2}|_i{}^j$ and $W_2^{0,2}|_i{}^j$ for this field are then measured over $n_\nu = 101$ values of threshold densities of $-3 \leqslant \nu \leqslant 4.5$. We repeat the measurements for smoothing scales $R_G = 15$, 20, 25, and $30\,h^{-1}$ Mpc.

To numerically extract the MTs from the density fields, we use the method developed in S. Appleby et al. (2018). Briefly, we construct an isofield triangulated surface mesh by generating a tetrahedral mesh from the pixels, and use the triangulated mesh and their unit normal vectors to construct the tensors (G. E. Schroder-Turk et al. 2013)

$$W_1^{0,2}|_i{}^j = \frac{1}{6V}\sum_t A_t \hat{n}_i \hat{n}^j, \tag{33}$$

$$W_2^{0,2}|_i{}^j = \frac{1}{3\pi V}\sum_k |\boldsymbol{e}_k|((\alpha_k + \sin\alpha_k)(\ddot{\boldsymbol{n}}_k^2)_i{}^j + (\alpha_k - \sin\alpha_k)(\dot{\boldsymbol{n}}_k^2)_i{}^j), \tag{34}$$

where the sum in Equation (33) is over all triangles in the surface mesh, $\hat{\boldsymbol{n}}_i$ is the corresponding unit normal vectors pointing externally to the surface, and A_t is the area of the tth triangle. In Equation (34), the sum is over k unique triangle edges in the mesh and $|\boldsymbol{e}_k|$ is the length of the kth edge. Each edge is shared by two triangles with unit normals $\hat{\boldsymbol{n}}_k$ and $\hat{\boldsymbol{n}}_k'$, α_e is the angle subtending these normals, and we define $\ddot{n}_k = (\hat{n}_k + \hat{\boldsymbol{n}}_k')/|\hat{n}_k + \hat{\boldsymbol{n}}_k'|$ and $\dot{n}_k = \ddot{n}_k \times \boldsymbol{e}_k$. The square of a vector in the above expression is shorthand for the symmetric tensor product and $V = (1000\,h^{-1}\,\mathrm{Mpc})^3$ is the total volume occupied by the field.

7. Numerical Reconstruction of Cumulants and Minkowski Tensors

First, we measure the two-point (σ, $\sigma_{1\perp}$, $\sigma_{1\parallel}$, $\sigma_{2\perp}$, and $\sigma_{2\parallel}$) and three-point ($\langle x^3\rangle$, $\langle xq_\perp^2\rangle$, $\langle xx_3^2\rangle$, $\langle x_3^2 J_{1\perp}\rangle$, and $\langle q_\perp^2 J_{1\perp}\rangle$) cumulants from the simulations, and compare them to the expected values computed according to the perturbative formalism of Section 5. The results are presented in Figure 1, as a function of smoothing scale R_G. The top left (right) panels are the two- (three-) point cumulants, the points and error bars are the mean and error on the mean measured from the snapshot boxes, respectively, while the dashed lines are obtained using perturbation theory. To calculate the cumulants using the results of Section 5 we adopt the input fiducial cosmological parameters and also take FOG velocity dispersion $\sigma_v = \sigma_B = 4.9\,h^{-1}$ Mpc. We explain how this value was determined in Appendix B. The agreement is excellent for all cumulants for scales $R_G \geqslant 20\,h^{-1}$ Mpc, with the three-point cumulants starting to deviate for $R_G \sim 15\,h^{-1}$ Mpc. In the bottom panels of Figure 1, we present the fractional difference between the measured and theoretical cumulants, divided by the theoretical prediction. The points and error bars are again the mean and error on the mean, respectively. We find percent-level agreement between theory and measurement for $R_G > 20\,h^{-1}$ Mpc, with a small (subpercent) systematic difference in the two-point cumulants (see bottom left panel) on large scales. We note that the three-point cumulants, divided by σ, are only very weakly sensitive to the smoothing scale R_G, a result that is consistent with T. Matsubara (2003) and S. Codis et al. (2013).

In Figure 2 we present measurements of the MT components $W_1^{0,2}|_1{}^1$ and $W_1^{0,2}|_3{}^3$ (green and red points and error bars) extracted from the $z = 1$ redshift-space snapshot boxes. The $W_1^{0,2}|_2{}^2$ component is statistically indistinguishable from $W_1^{0,2}|_1{}^1$ and not plotted, and all off-diagonal elements are consistent with zero and also not plotted. Each panel corresponds to a different smoothing scale $R_G = 15$, 20, 25, and $30\,h^{-1}$ Mpc. The black dashed lines are the corresponding theoretical expectation values $\langle w_1{}^1 + w_2{}^2\rangle/2$ and $\langle w_3{}^3\rangle$ from Equation (14) using the two- and three-point cumulants inferred from perturbation theory. The faint gray dotted lines are the Gaussian limits of the perturbation theory predictions $\langle w_1{}^1 + w_2{}^2\rangle_G/2$ and $\langle w_3{}^3\rangle_G$, obtained by setting all three-point cumulants to zero. The agreement between perturbation theory and measurements (black dashed lines and green and red points, respectively) is good for scales $R_G > 20\,h^{-1}$ Mpc, but higher-order contributions increasingly modify the shape of the curves on smaller scales (cf top left panel). For large negative thresholds, the ensemble average predicts that $\langle w_i{}^i\rangle$ is negative, despite these quantities being positive definite by definition. This indicates a failure of both perturbation theory and the Edgeworth expansion in this regime, to the order at which we are working. The small-scale breakdown of perturbation theory is clearly presented in the lower panels of Figure 1, where the theoretical predictions depart from the measured values of the cumulants for $R_G < 20\,h^{-1}$ Mpc. This is particularly apparent for the bispectrum components x^3, xx_3^2, and $xq_\perp^2$ (see bottom right panel). Independently, the breakdown of the Edgeworth expansion is a known phenomenon (E. Sellentin et al. 2017), and can lead to spurious negative PDFs and summary statistics, as we see in the top panels of Figure 2. The breakdown of the Edgeworth expansion can be studied using fields for which nonperturbatively non-Gaussian analytic results are known (F. Bernardeau & C. Pichon 2024; R. C. Bernardo et al. 2026).

In Figure 3 we present the difference between the measured values of the MT components and the Gaussian expectation values (green and red dashed lines, respectively). We present the error on the mean as a shaded region around the dashed lines; its width is comparable to the thickness of the lines. The solid green and red lines are, respectively, the residuals between the predictions (Equation (14)) and their Gaussian limit with all cubic cumulants zero. We observe a characteristic pattern in the residuals, which predominantly arises due to the odd Hermite polynomials $H_1(\nu)$ and $H_3(\nu)$. The agreement between the prediction and measurements (solid and dashed lines, respectively) improves as the smoothing scale increases. However, we do not expect these curves to agree exactly, as the measured components (dashed lines) also contain all higher-point information whereas the analytic calculation is truncated at the three-point level. The difference between the solid and dashed curves is predominantly due to the four-point cumulants, and should be accounted for when performing cosmological parameter estimation using the MTs. Ideally one would like to express the quartic cumulants in terms of the trispectrum using perturbation theory, in which case the four-point contributions could also be leveraged to constrain cosmological parameters. However, in lieu of an analytic prediction for the higher-order cumulants, one approach would be to include additional Hermite coefficients as free parameters and marginalize over

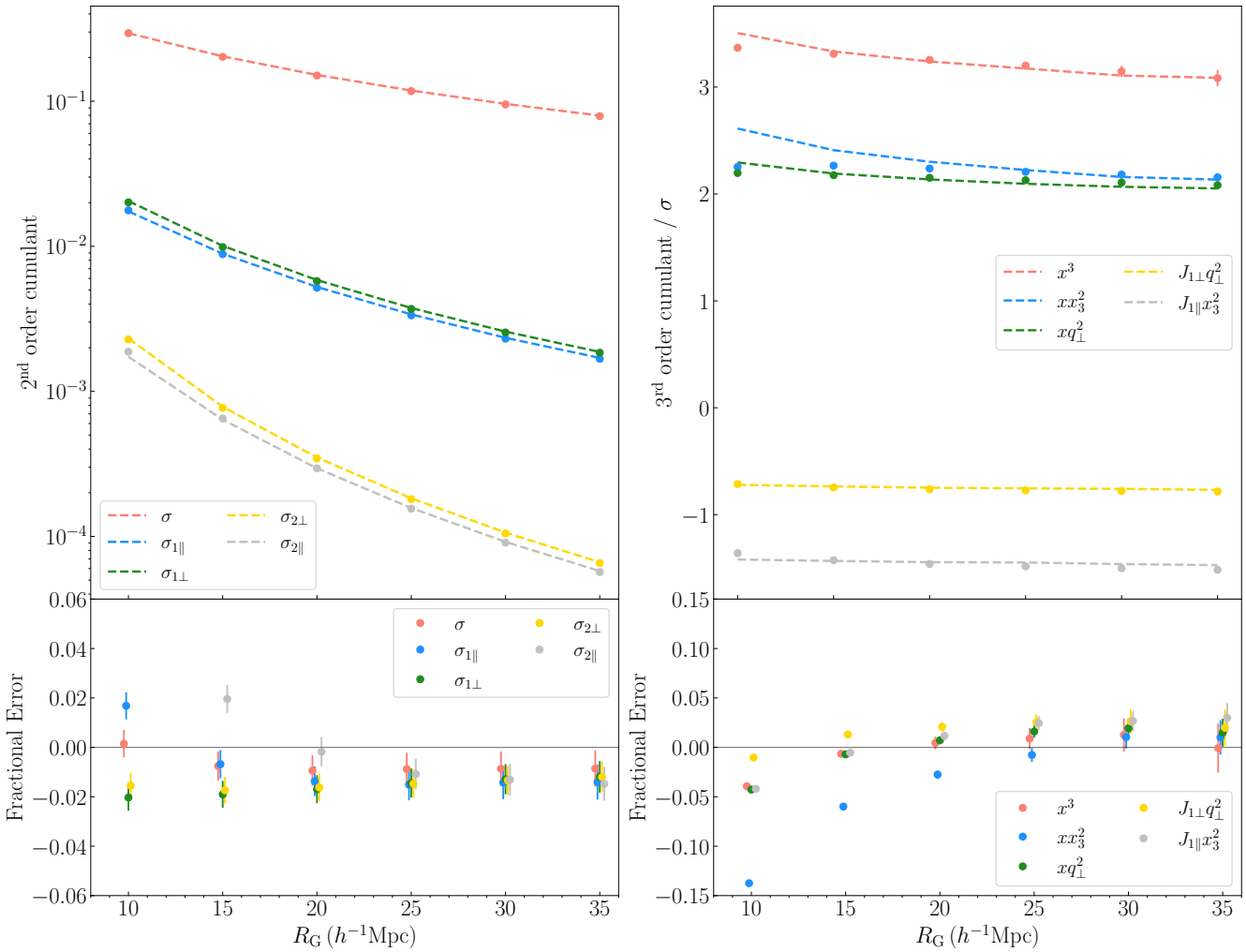

Figure 1. Top panels: numerically measured two-point (left panel) and three-point (right panel) cumulants from a set of $z = 1$ dark matter snapshot boxes in redshift space (points and error bars). The dashed lines are the corresponding ensemble expectation values constructed in Section 5, taking $\sigma_v = \sigma_B = 4.9\,h^{-1}$ Mpc. Error bars are the error on the mean. The scaling of most cumulants is well captured by perturbation theory, notwithstanding a small departure at smaller scales for xx_3^2. Bottom panels: fractional uncertainty between the measured and theoretical estimates of the two-point (left panel) and three-point (right panel) cumulants. The agreement is percent level for $R_G > 20\,h^{-1}$ Mpc.

them. For example one could fit the following function to measured $W_1^{0,2}$ curves:

$$\langle w_1{}^1\rangle + \langle w_2{}^2\rangle = \frac{\sigma_{1\perp}e^{-\nu^2/2}}{6\pi\sigma}\left[A_{G\perp}^{(1)}\left(H_0(\nu) + \frac{\langle x^3\rangle}{6}H_3(\nu)\right) + (B_\perp^{(1)}\langle xq_\perp^2\rangle + C_\perp^{(1)}\langle xx_3^2\rangle)H_1(\nu) + h_{6\perp}H_6(\nu) + h_{4\perp}H_4(\nu) + h_{2\perp}H_2(\nu)\right], \tag{35a}$$

$$\langle w_3{}^3\rangle = \frac{\sigma_{1\perp}e^{-\nu^2/2}}{6\pi\sigma}\left[A_{G\parallel}^{(1)}\left(H_0(\nu) + \frac{\langle x^3\rangle}{6}H_3(\nu)\right) + (B_\parallel^{(1)}\langle xq_\perp^2\rangle + C_\parallel^{(1)}\langle xx_3^2\rangle)H_1(\nu) + h_{6\parallel}H_6(\nu) + h_{4\parallel}H_4(\nu) + h_{2\parallel}H_2(\nu)\right], \tag{35b}$$

where $h_{2,4,6\perp}$ and $h_{2,4,6\parallel}$ are free parameters to be marginalized over.[12] This would account for the contribution of the fourth-order cumulants to the shape of $W_1^{0,2}$, and higher-order contributions could be similarly accounted for at a cost of increasing the number of nuisance parameters $h_{i\perp}$ and $h_{i\parallel}$. The underlying point is that setting all higher-order cumulants to zero in the ensemble average will lead to a worse fit and potentially parameter biases. A more detailed exploration of this issue will be pursued in future work.

In Figures 4 and 5, we present the same results as Figures 2 and 3, respectively, but for the second MT $W_2^{0,2}$ and the corresponding ensemble averages in Section 4.2. We observe a very similar picture: perturbation theory performs well for

[12] This approach is complicated by the fact that the quartic cumulants will also contribute a correction to the coefficients of $H_0(\nu)$, i.e., the amplitude of the MT curves. Additional terms $h_{0\perp}H_0(\nu)$ and $h_{0\parallel}H_0(\nu)$ could also be included, although the prior ranges of $h_{0\perp}$ and $h_{0\parallel}$ should be carefully restricted.

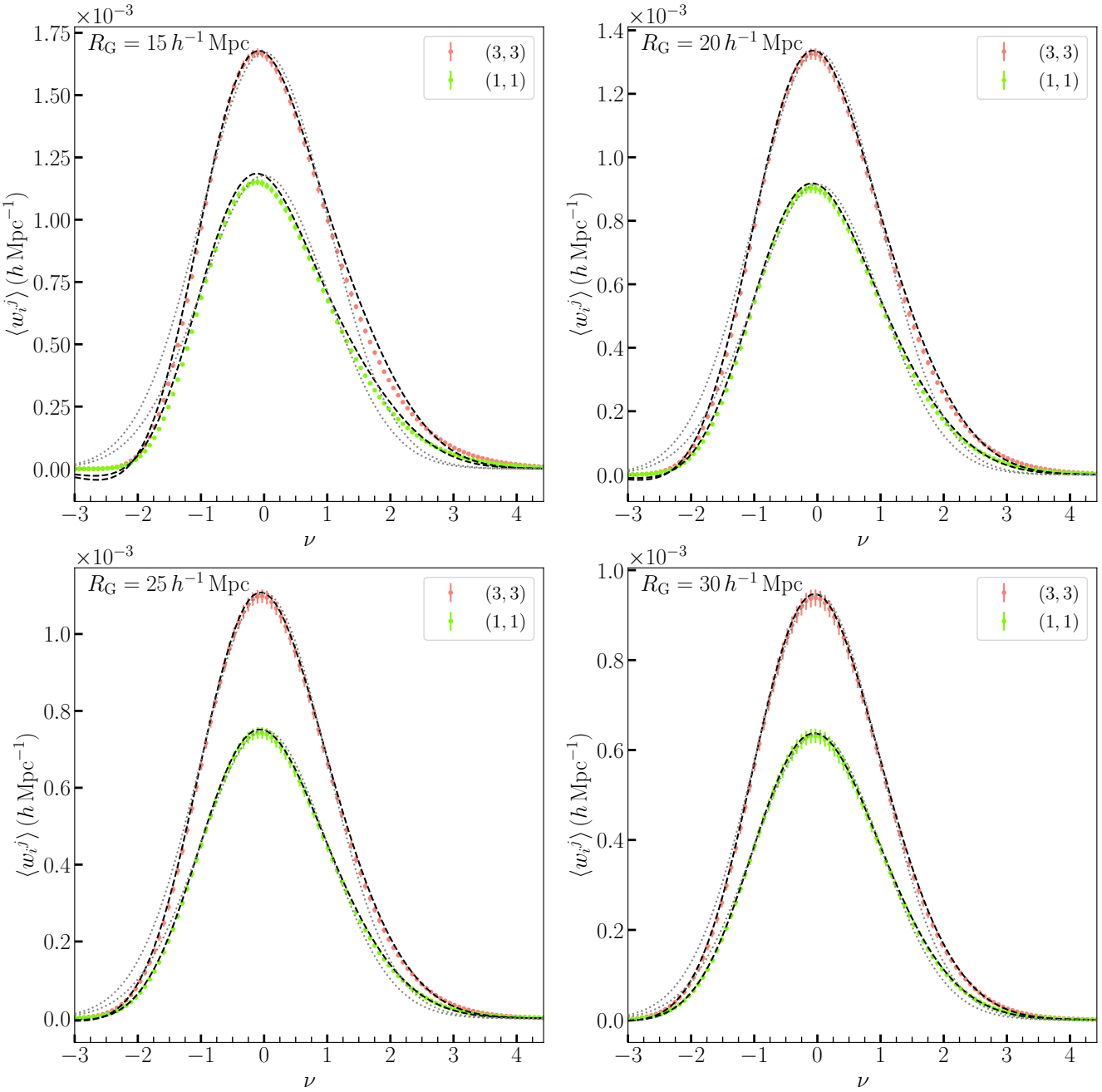

Figure 2. The MT components $W_1^{0,2}|_1{}^1$ and $W_1^{0,2}|_3{}^3$ (green and red points and error bars, respectively) extracted from $N = 100$ realizations of Quijote $z = 1$ dark matter snapshot boxes in redshift space. The black dashed lines are the theoretical predictions for the ensemble averages $\langle w_1{}^1 \rangle$ and $\langle w_3{}^3 \rangle$ inferred from Section 4.1, with FOG velocity dispersion $\sigma_v = \sigma_B = 4.9\,h^{-1}$ Mpc. The gray dotted lines are the Gaussian predictions $\langle w_1{}^1 \rangle_G$ and $\langle w_3{}^3 \rangle_G$ with the same FOG velocity dispersion included. The top left and right panels correspond to smoothing scales $R_G = 15$ and $20\,h^{-1}$ Mpc, respectively, and the bottom left and right panels to $R_G = 25$ and $30\,h^{-1}$ Mpc, respectively. On the range of considered scales, the non-Gaussian features are significant and well captured by perturbation theory. See also Figure 7 without the FOG correction.

$R_G \geqslant 20\,h^{-1}$ Mpc, but higher-order contributions increasingly impact the components on smaller scales. The residuals in Figure 5 are now dominated by the even Hermite polynomials $H_0(\nu)$, $H_2(\nu)$, and $H_4(\nu)$.

The figures illustrate the success for perturbation theory and the Edgeworth expansion, showing a good match between the ensemble average and measurements from simulations. In contrast, in Figures 7 and 8 we present the same measurements, but now the theoretical predictions for $\langle w_i{}^i \rangle$ and $\langle \nu_i{}^i \rangle$ and their Gaussian limits (see the black dashed and gray dotted lines, respectively) are constructed by setting $\sigma_v = \sigma_B = 0$. Now, we see that perturbation theory performs significantly worse for the (3, 3) component of the statistics (cf red points and error bars), except when smoothing on the largest scales of $R_G = 30\,h^{-1}$ Mpc. In contrast, the components perpendicular to the line of sight (green points) remain well described by perturbation theory and are not strongly affected by the FOG effect. It is clear that the components of the field parallel to the line of sight are significantly contaminated by nonlinear velocity dispersion effects, a result also noted in S. Appleby et al. (2022a). Whether this is positive or negative depends on

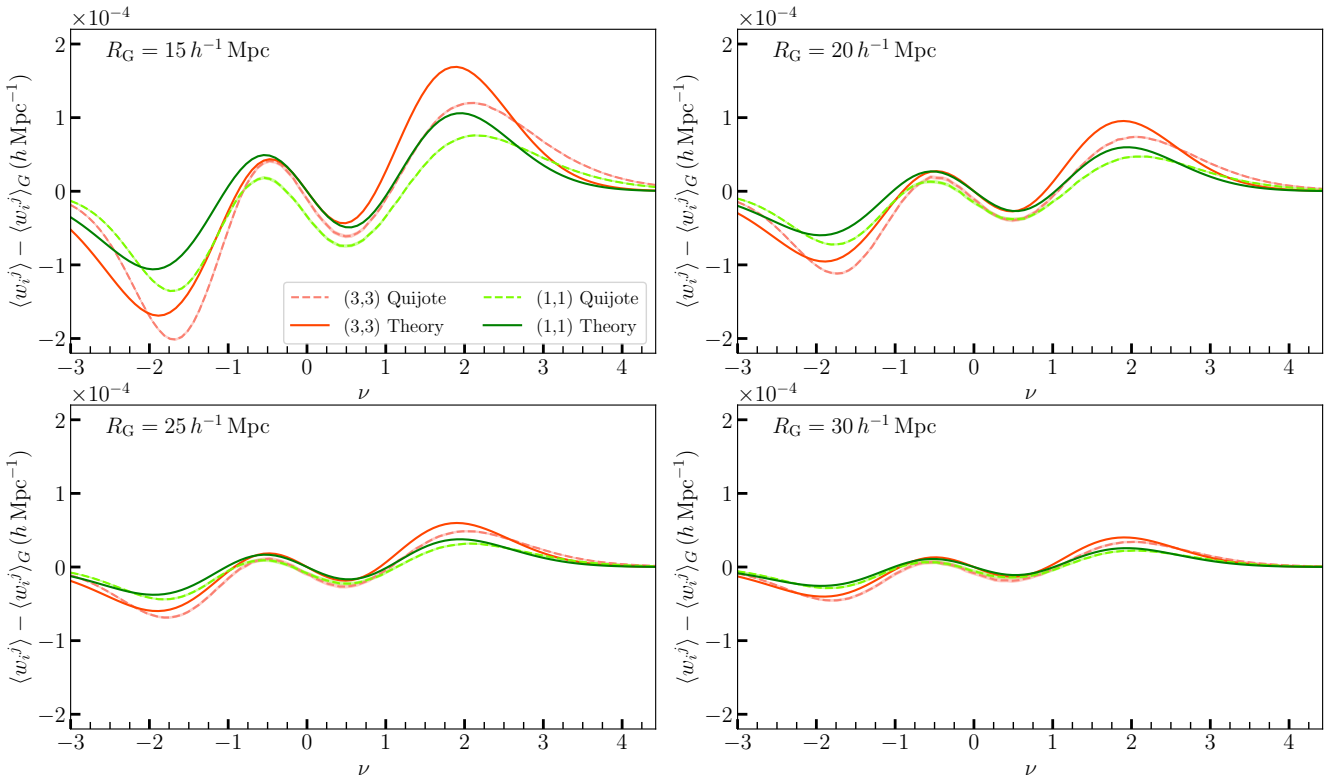

Figure 3. Residuals $W_1^{0,2}|_i{}^i - \langle w_i{}^i\rangle_G$ (red and green dashed lines) and $\langle w_i{}^i\rangle - \langle w_i{}^i\rangle_G$ (red and green solid lines), where $W_1^{0,2}|_i{}^i$ is the mean value of the MT components from the snapshot boxes, $\langle w_i{}^i\rangle$ is the non-Gaussian prediction obtained in this work, and $\langle w_i{}^i\rangle_G$ the Gaussian limit of the prediction. The residuals are dominated by the odd Hermite polynomials $H_1(\nu)$ and $H_3(\nu)$. As expected the larger the smoothing scale, the better the match and the smaller the amplitude.

whether we are interested in modeling the FOG effect, or if we consider it a contaminant to cosmological parameter estimation. Also, we note that the FOG effect will be more pronounced in dark matter fields compared to galaxies: dark matter particles generally exhibit larger stochastic velocities. Hence this work can be considered as a worst case scenario. In the future we will extract the MTs from galaxy fields and consider the effect of galaxy bias, shot noise, and FOG velocity dispersion.

In a number of previous works, it was proposed that redshift-space distortion information can be extracted from the scalar Minkowski functionals by creating two-dimensional slices of galaxy data in planes, rotating the direction of the plane relative to the line of sight, and measuring variations in the two-dimensional scalar statistics (T. Matsubara 1996; S. Codis et al. 2013). While this approach would certainly yield directional information, the MTs represent a more comprehensive and natural method for extracting anisotropic signals. There are two primary advantages to using the MTs. First, the tensors contain additional information in their off-diagonal elements and if the density field exhibits anisotropy beyond the known redshift-space distortion correction, it will present as nonzero off-diagonal elements. This information would not be present in the scalar functionals.

Second, the actual redshift-space distortion effect is radial and not plane parallel. This is particularly important for modern galaxy surveys, which cover a significant fraction of the sky. We cannot construct a plane that is globally parallel to the line of sight, but the issue is naturally resolved by using the MTs in a spherical coordinate system, as detailed in S. Appleby et al. (2022a). The Cartesian components constructed in this work can be simply adapted to a spherical coordinate system, by defining a coordinate system at each point in the space that is locally aligned to the line of sight and then averaging over the entire volume.

8. Discussion

MTs are a geometrical tool for analyzing the anisotropic information embedded in cosmic structures, especially those affected by redshift-space distortions. By incorporating a perturbative non-Gaussian Edgeworth expansion (up to cubic-order cumulants of the redshift-space density field and its derivatives), the derived MTs can also capture the morphological evolution of the matter distribution in the weakly nonlinear regime, hence improving constraints on cosmological parameters. This provides a pathway for using ongoing (e.g., DESI and Euclid) and upcoming (LSST and Nancy Grace Roman Space Telescope) galaxy surveys to infer properties of the underlying cosmology and its cosmic evolution.

In this work we have calculated the ensemble average of the translation-invariant MTs $W_1^{0,2}$ and $W_2^{0,2}$ in redshift space to leading order in a non-Gaussian expansion of the PDF of the field and its first and second derivatives. Starting from the definitions of $W_1^{0,2}$ and $W_2^{0,2}$, we utilized the assumed statistical homogeneity of the fields to approximately equate volume and ensemble averages. The ensemble average was then constructed using the Edgeworth expansion of the PDF of the fields, truncated at the level of the three-point cumulants. We estimated the two- and three-point cumulants using standard perturbation theory in redshift space.

The main results of this work are Equations (14) and (21), which express the ensemble averages of the MT components in terms of Hermite polynomials, a set of coefficients which are functions of $\lambda = \sigma_{1\parallel}/\sigma_{1\perp}$ only, and two- and three-point field cumulants. To

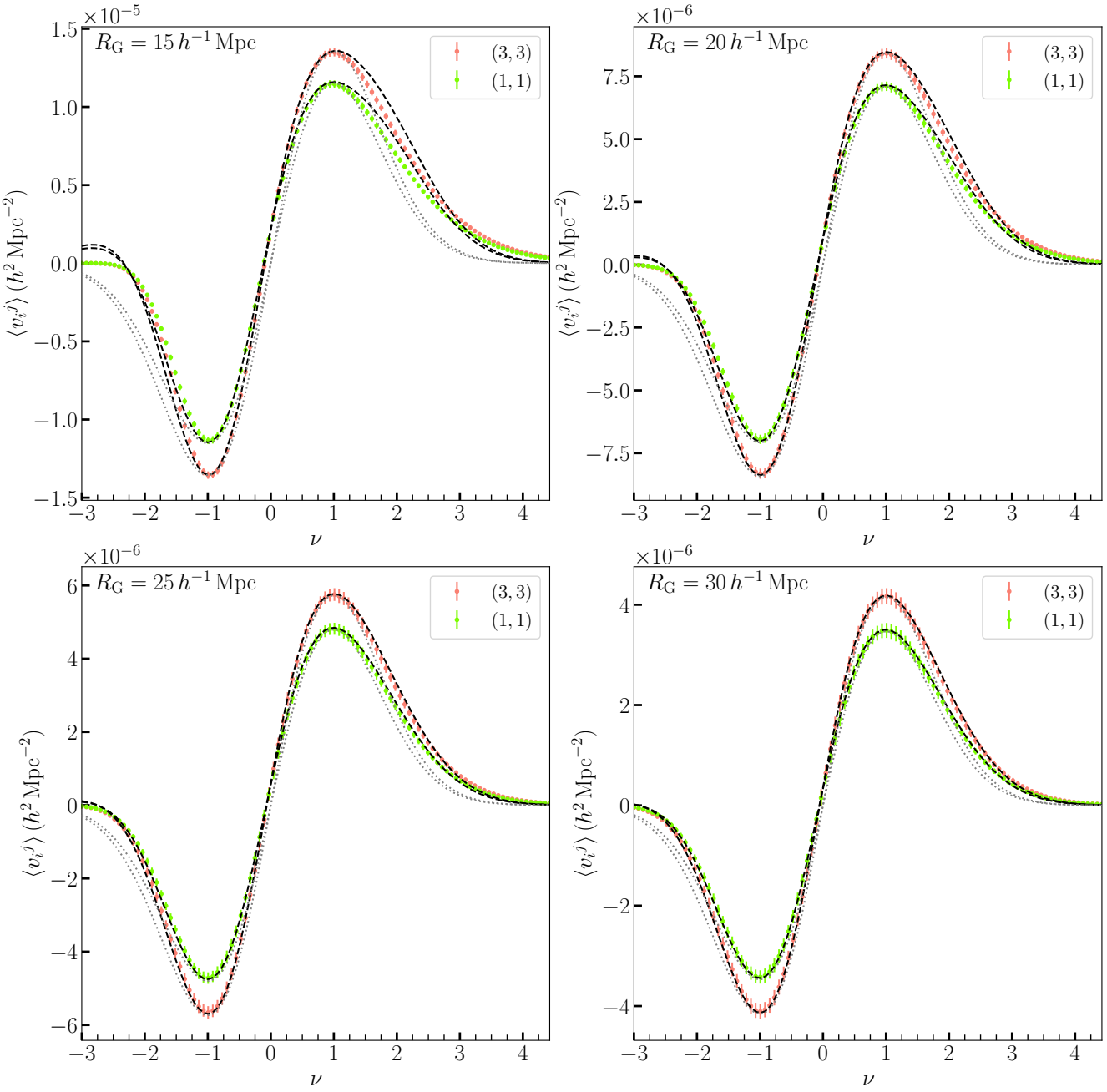

Figure 4. The MT components $W_2^{0,2}|_{\mathrm{l}}{}^1$ and $W_2^{0,2}|_3{}^3$ (green and red points and 1σ error bars, respectively) extracted from $N = 100$ realizations of Quijote $z = 1$ dark matter snapshot boxes in redshift space. The black dashed lines are the theoretical predictions for the ensemble averages $\langle v_1{}^1 \rangle$ and $\langle v_3{}^3 \rangle$ inferred from Section 4.2, with FOG velocity dispersion $\sigma_v = \sigma_B = 4.9\,h^{-1}$ Mpc. The gray dotted lines are the Gaussian predictions with the same FOG velocity dispersion included. The top left and right panels correspond to smoothing scales $R_G = 15$ and $2\,h^{-1}$ Mpc, respectively, and the bottom left and right panels to $R_G = 25$ and $30\,h^{-1}$ Mpc, respectively. As for $W_1^{0,2}|_i{}^i$ (Figure 2), the components $W_2^{0,2}|_{\mathrm{l}}{}^1$ display an informative non-Gaussian signature, which are best captured by perturbation theory on larger scales.

calculate the analytic predictions for a given cosmology, one should construct the linear matter power spectrum $P_m(k, z)$ using, e.g., CAMB, perform the two-point (Equations (24)) and three-point (Equations (26)) cumulant integrals, and use them in our expressions for the ensemble averages $\langle w_i{}^j \rangle$ and $\langle v_i{}^j \rangle$.

We tested the analytic expressions for $\langle w_i{}^j \rangle$ and $\langle v_i{}^j \rangle$ by extracting the MTs from $z = 1$ dark matter snapshot boxes using the Quijote simulation suite. We find reasonable agreement between the measured volume averages and predicted ensemble averages when we smooth the field on scales $R_G > 20\,h^{-1}$ Mpc, although we must include a parameterization to account for the FOG effect. This latter phenomenon significantly impacts the components of the tensor parallel to the line of sight, and requires an additional free parameter to model. This will partially confound our ultimate goal of constraining cosmological parameters.

By moving beyond the Gaussian limit, the information content of the MT curves is manifested. The Gaussian information is contained in the amplitudes of $W_1^{0,2}$ and $W_2^{0,2}$ (coefficients of H_0 and H_1, respectively), which are functions of the ratio $\sigma_{1\perp}/\sigma$ and coefficients involving $\lambda = \sigma_{1\parallel}/\sigma_{1\perp}$, which is also a ratio. Hence they contain information relating to the shape of the power

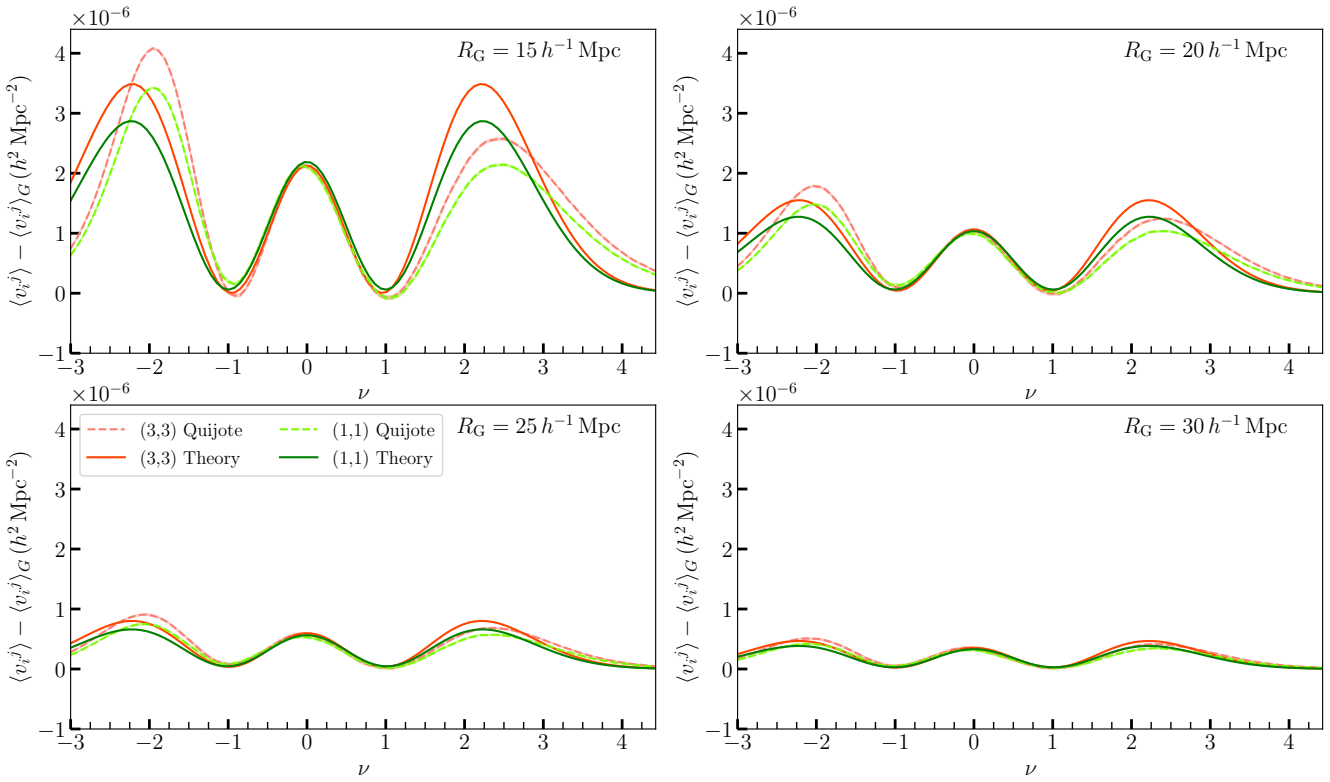

Figure 5. Residuals $W_2^{0,2}|_i{}^i - \langle v_i{}^i\rangle_G$ (red and green dashed lines) and $\langle v_i{}^i\rangle - \langle v_i{}^i\rangle_G$ (red and green solid lines), where $W_2^{0,2}|_i{}^i$ is the mean value of the MT components from the snapshot boxes, $\langle v_i{}^i\rangle$ is the non-Gaussian prediction obtained in this work, and $\langle v_i{}^i\rangle_G$ the Gaussian limit of the prediction. The residuals are dominated by the even Hermite polynomials $H_0(\nu)$, $H_2(\nu)$, and $H_4(\nu)$. Qualitatively, the same convergence is observed as in Figure 3 for $W_1^{0,2}|_i{}^i$.

spectrum: predominantly the parameters Ω_m and n_s, and also the growth rate $\beta = f/b$. Specifically, the amplitude of the density fluctuations $b_1\sigma_8$ cannot be extracted from the Gaussian part. However, by measuring the skewness of the MT curves, the cubic cumulants $\langle x^3\rangle/\sigma^3$, etc., are proportional to $b_1\sigma_8$, so the combined measurement of the Gaussian and non-Gaussian information will provide joint constraints on $f\sigma_8$ and $b_1\sigma_8$.

The statistics considered in this work are tensors, and we utilized Cartesian coordinates aligned with the line of sight between the observer and the density field and further assumed the plane-parallel approximation. The latter condition makes the simplifying assumption that the line-of-sight vector is parallel at every point in the density field. In reality the redshift-space distortion operator is radial relative to the observer position, and great care should be taken with coordinate systems when extracting these statistics from galaxy data. This issue was the focus of the work of S. Appleby et al. (2022a), with the conclusion that spherical coordinate systems should be used when measuring the MTs. In the Cartesian basis used in this work, the tensors are diagonal; they would also be diagonal in any rotated coordinate system that preserves the line-of-sight direction due to the statistical isotropy in the plane perpendicular to $\boldsymbol{e}_3$. We could potentially use the invariance of the MTs to this subset of rotations to test statistical isotropy in the $(\boldsymbol{e}_1, \boldsymbol{e}_2)$ plane. However, testing isotropy perpendicular to the line of sight is a subtle problem due to the fact that the subspace is S^2 not $\mathbb{R}^2$, and will be considered elsewhere.

Throughout this work we have focused on the rank-2 quantities $W_1^{0,2}$ and $W_2^{0,2}$. An interesting future direction would be to study the higher-rank statistics involving increasing tensor products of $\hat{n} \otimes \hat{n} \otimes \hat{n} \otimes \ldots$. The higher-rank tensors could be similarly Edgeworth expanded, and would yield different combinations of cumulants and Hermite polynomials while simultaneously probing a higher multipole expansion of the random shapes generated by the isofield surfaces of random fields.

The Minkowski functionals and tensors contain complementary information relative to two-point function analyses (correlation function and power spectrum), and can be measured in conjunction with those statistics to improve existing parameter constraints. Although the Edgeworth expansion has only been utilized to cubic order in redshift space (S. Codis et al. 2013; and quartic in real space; C. Gay et al. 2012; T. Matsubara et al. 2020), we can proceed to higher orders with relative ease, limited only by our ability to express the higher-point cumulants using perturbation theory, performing the higher-dimensional integrations necessary to obtain the n-point cumulants $\langle x^n\rangle$, etc.

This work serves as a precursor to extracting the MTs from current and future galaxy catalogs, and subsequently performing cosmological parameter estimation. Principally our goal will be to infer $f\sigma_8$ and $b\sigma_8$, and by making repeated measurements at different redshifts, potentially placing constraints on the growth rate (C. Gay et al. 2012). Note that this inference will undoubtedly have different biases compared to alternative methods such as weak lensing (M. Yamamoto et al. 2025) or baryonic acoustic oscillations (M. Abdul-Karim et al. 2025). Hence MT should be implemented to leverage such biases. The application of our results to data will be pursued in future work.

Acknowledgments

S.A. is supported by an appointment to the JRG Program at the APCTP through the Science and Technology Promotion Fund and Lottery Fund of the Korean Government, and was also supported by the Korean Local Governments in Gyeongsangbuk-do Province and Pohang City. C.P. thanks Katarina Kraljic for feedback. C.P. is partially supported by the grant SEGAL[13] ANR-19-CE31-0017 of the French Agence Nationale de la Recherche. C.B.P. is supported by KIAS Individual grants (PG016903) at the Korea Institute for Advanced Study, and is also supported by the National Research Foundation of Korea (NRF) grant funded by the Korean government (MSIT; RS-2024-00360385).

Appendix A
Isotropic Limit

In the main body of the text we constructed the ensemble averages of the MTs in redshift space. Here we show that in the isotropic limit, the traces of these quantities reduce to the W_1 and W_2 presented in T. Matsubara (2003). The isotropic limit corresponds to taking $\lambda \to (1/\sqrt{2})^+$ and $\sigma_v = \sigma_B = 0$, and the cumulants take values $\sigma^2 = \sigma_0^2, \sigma_{1\parallel}^2 = \sigma_1^2/3, \sigma_{1\perp}^2 = 2\sigma_1^2/3, \sigma_{2\perp}^2 = 8\sigma_2^2/15, \sigma_{2\parallel}^2 = \sigma_2^2/5$, and $\sigma_Q^2 = 2\sigma_2^2/15$. We also have the following three-point isotropic limits:

$$\langle x^3\rangle = \frac{\langle\delta^3\rangle}{\sigma_0^3},\ \langle x q_\perp^2\rangle = \langle x x_3^2\rangle = \frac{\langle\delta|\nabla\delta|^2\rangle}{\sigma_0\sigma_1^2},\ \frac{\langle q_\perp^2 J_{1\perp}\rangle}{\gamma_\perp} = \frac{3\langle|\nabla\delta|^2\nabla^2\delta\rangle\sigma_0}{4\sigma_1^4},\ \frac{\langle x_3^2 J_{1\perp}\rangle}{\gamma_\perp} = \frac{3\langle|\nabla\delta|^2\nabla^2\delta\rangle\sigma_0}{2\sigma_1^4}. \tag{A1}$$

Taking $\lambda \to (1/\sqrt{2})^+$, we have

$$\begin{aligned}
&A_{G\perp}^{(1)} \to 2\sqrt{2}/3,\quad B_\perp^{(1)} \to 6\sqrt{2}/15,\quad C_\perp^{(1)} \to -\sqrt{2}/15, A_{G\parallel}^{(1)} \to \sqrt{2}/3,\quad B_\parallel^{(1)} \to -\sqrt{2}/15,\quad C_\parallel^{(1)} \to 7\sqrt{2}/30,\\
&A_{G\perp}^{(2)} \to 4/3,\quad B_\perp^{(2)} \to 16/15,\quad C_\perp^{(2)} \to 4/15,\quad D_\perp^{(2)} \to -12/15,\quad E_\perp^{(2)} \to -4/15,\\
&A_{G\parallel}^{(2)} \to 2/3,\quad B_\parallel^{(2)} \to 4/15,\quad C_\parallel^{(2)} \to 6/15,\quad D_\parallel^{(2)} \to 2/15,\quad E_\parallel^{(2)} \to -6/15.
\end{aligned}$$

Inserting these into Equations (14) and (21) we have

$$\langle w_1{}^1\rangle + \langle w_2{}^2\rangle = \frac{2\sigma_1}{9\sqrt{3}\,\pi\sigma_0} e^{-\nu^2/2}\left[H_0(\nu) + \frac{1}{6}\frac{\langle\delta^3\rangle}{\sigma_0^3}H_3(\nu) + \frac{1}{2}\frac{\langle\delta|\nabla\delta|^2\rangle}{\sigma_0\sigma_1^2}H_2(\nu) + \mathcal{O}(\sigma_0^2)\right], \tag{A3a}$$

$$\langle w_3{}^3\rangle = \frac{\sigma_1}{9\sqrt{3}\,\pi\sigma_0} e^{-\nu^2/2}\left[H_0(\nu) + \frac{1}{6}\frac{\langle\delta^3\rangle}{\sigma_0^3}H_3(\nu) + \frac{1}{2}\frac{\langle\delta|\nabla\delta|^2\rangle}{\sigma_0\sigma_1^2}H_2(\nu) + \mathcal{O}(\sigma_0^2)\right], \tag{A3b}$$

and

$$\langle v_1{}^1\rangle + \langle v_2{}^2\rangle = \frac{2\sigma_1^2}{27\pi\sqrt{2\pi}\,\sigma_0^2} e^{-\nu^2/2}\left[H_1(\nu) + \frac{1}{6}\frac{\langle\delta^3\rangle}{\sigma_0^3}H_4(\nu) + \frac{\langle\delta|\nabla\delta|^2\rangle}{\sigma_0\sigma_1^2}H_2(\nu) - \frac{3}{4}\frac{\langle|\nabla\delta|^2\nabla^2\delta\rangle\sigma_0}{\sigma_1^4}H_0(\nu) + \mathcal{O}(\sigma_0^2)\right], \tag{A4a}$$

$$\langle v_3{}^3\rangle = \frac{\sigma_1^2}{27\pi\sqrt{2\pi}\,\sigma_0^2} e^{-\nu^2/2}\left[H_1(\nu) + \frac{1}{6}\frac{\langle\delta^3\rangle}{\sigma_0^3}H_4(\nu) + \frac{\langle\delta|\nabla\delta|^2\rangle}{\sigma_0\sigma_1^2}H_2(\nu) - \frac{3}{4}\frac{\langle|\nabla\delta|^2\nabla^2\delta\rangle\sigma_0}{\sigma_1^4}H_0(\nu) + \mathcal{O}(\sigma_0^2)\right]. \tag{A4b}$$

The traces yield, respectively, the Minkowski functionals W_1 and W_2 in T. Matsubara (2003).

The ensemble average of the Minkowski functional W_1 has been constructed in redshift space in S. Codis et al. (2013); we can also compare the trace $\mathrm{Tr}\langle w_i{}^j\rangle$ obtained in this work to that result; specifically $\mathcal{N}_3$ as defined in Equations (47) and (48) of S. Codis et al. (2013). To make the comparison, we fix $\sigma_v = \sigma_B = 0$ since the FOG was not included in that work, and we divide $\mathcal{N}_3$ by 6 to match definitions. The resulting ensemble averages of $\mathrm{Tr}\langle w_i{}^j\rangle$ and $\mathcal{N}_3/6$ are presented in the left panel of Figure 6, where the four sets of curves correspond to $R_G = 15$, 20, 25, and $30\,h^{-1}$ Mpc. The black solid and yellow dashed lines representing the statistics are in excellent agreement, which serve as a consistency check of our calculation.

[13] https://www.secular-evolution.org

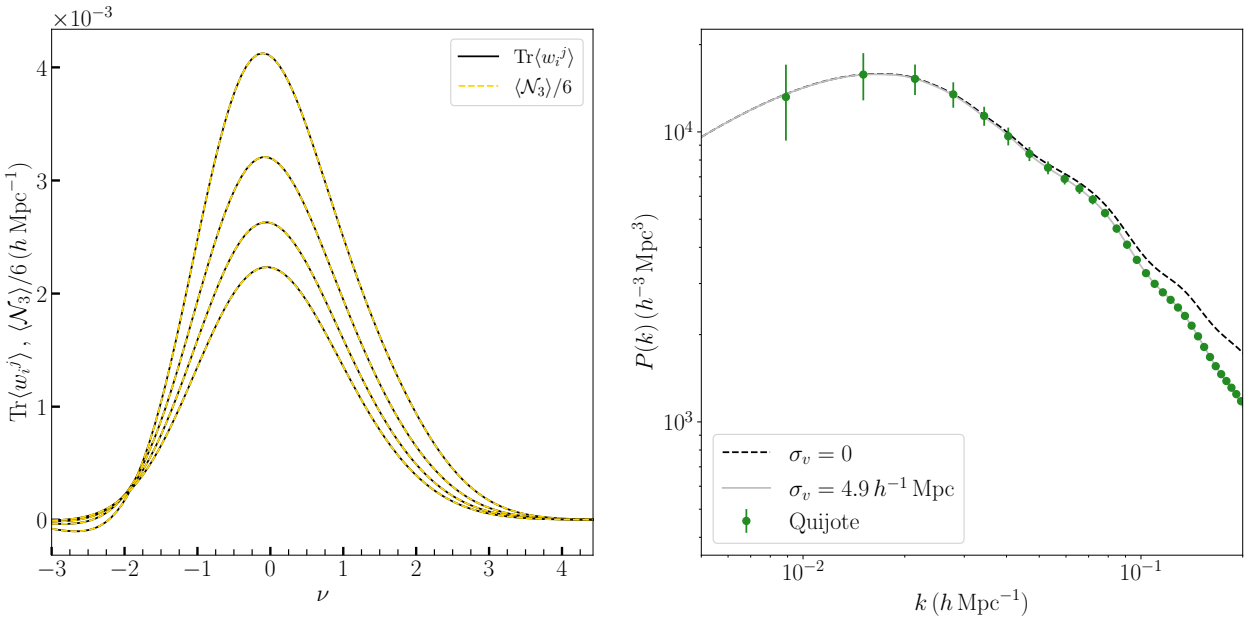

Figure 6. Left panel: a comparison of the trace of ${w_i}^j$ calculated in this work (black solid lines) and the total area of isofield surfaces $\mathcal{N}_3$ in S. Codis et al. (2013, yellow dashed lines). The curves in descending amplitude are for smoothing scales $R_G = 15$, 20, 25, and 30 h^{-1} Mpc. Right panel: the redshift-space power spectrum of $z = 1$ fiducial cosmology Quijote snapshot boxes (green points and error bars) and the perturbation theory expectation value with zero velocity dispersion (black dashed line) and with the best-fit $\sigma_v = 4.9\,h^{-1}$ Mpc (gray solid line).

Appendix B
Finger-of-God Velocity Dispersion

In the main body of the text, we use velocity dispersion values $\sigma_v = \sigma_B = 4.9\,h^{-1}$ Mpc. In this section we briefly review how this value has been determined. In the literature the parameters σ_v and σ_B are sometimes treated as independent parameters to be jointly constrained, but in this work we always fix them to be equal. We also note that the choice of exponential function to describe the FOG effect is not necessarily applicable over all scales, and in fact on smaller scales the exponential damping is too steep. Improved modeling of this phenomenon on small scales will be considered elsewhere.

To estimate σ_v, we take $N_{\rm real} = 4000$ measurements of the dark matter power spectrum (monopole) extracted from the $z = 1$, redshift-space distorted fiducial Quijote simulations. The measurements are made over $N_{\rm b} = 31$ fourier mode bins from $9 \times 10^{-3}\,h\,\mathrm{Mpc}^{-1} < k < 0.20\,h\,\mathrm{Mpc}^{-1}$. From these realizations we construct a covariance matrix for the power spectrum, which we denote Σ_{ij}, where the i and j subscripts run over the k bins. We then take a different set of $N = 500$ realizations and measure the mean power spectrum in the 31 Fourier bins: this is our data vector, which we denote as $\bar{P}_i$. To this power spectrum, we fit the following functional form:

$$P_i = \frac{1}{2}\int_{-1}^{1} d\mu P(\mu, k_i) = \frac{1}{2}\int_{-1}^{1} d\mu [P_{00} + \mu^2(2P_{01} + P_{02} + P_{11}) + \mu^4(P_{03} + P_{04} + P_{12} + P_{13} + P_{22}/4)], \tag{B1}$$

which is derived using the combined distribution function and Eulerian perturbation theory approach of P. McDonald (2011), U. Seljak & P. McDonald (2011), Z. Vlah et al. (2012), T. Okumura et al. (2012a, 2012b), and S. Saito et al. (2014). We direct the reader to those works and C. Howlett (2019, Appendix A) for the exact definitions of the P_{mn} contributions and corresponding kernels. We fix all cosmological parameters to their correct, fiducial values, and fit a single parameter, σ_v, to the power spectrum by minimizing

$$\chi^2 = [\bar{P}_i - P_i]\Sigma_{ij}^{-1}[\bar{P}_j - P_j]. \tag{B2}$$

The resulting best fit is given by $\sigma_v = 4.90 \pm 0.04\,h^{-1}$ Mpc, which is the value that is adopted in this work. In the right panel of Figure 6 we present the $z = 1$, redshift-space power spectrum measured from the Quijote simulations (green points and error bars), and the perturbation theory predictions with $\sigma_v = 0$ and $\sigma_v = 4.90\,h^{-1}$ Mpc (black dashed and solid gray lines, respectively).

To obtain the best-fit σ_v velocity dispersion, we have measured the power spectrum shape on large scales under the assumption that cosmological parameters are known and fixed. In practice, this is not an approach that could be used for realistic data. Instead, one should simultaneously fit σ_v and the cosmological parameters using a large array of summary statistics, potentially including the power spectrum, Minkowski functionals, tensors, etc. Alternatively, one could measure the galaxy correlation function on small scales to infer σ_v.

To show the corresponding FOG effect on the statistics used in this work, in Figures 7 and 8 we present the MT predictions without the FOG effect accounted for, that is we set $\sigma_v = \sigma_B = 0$.

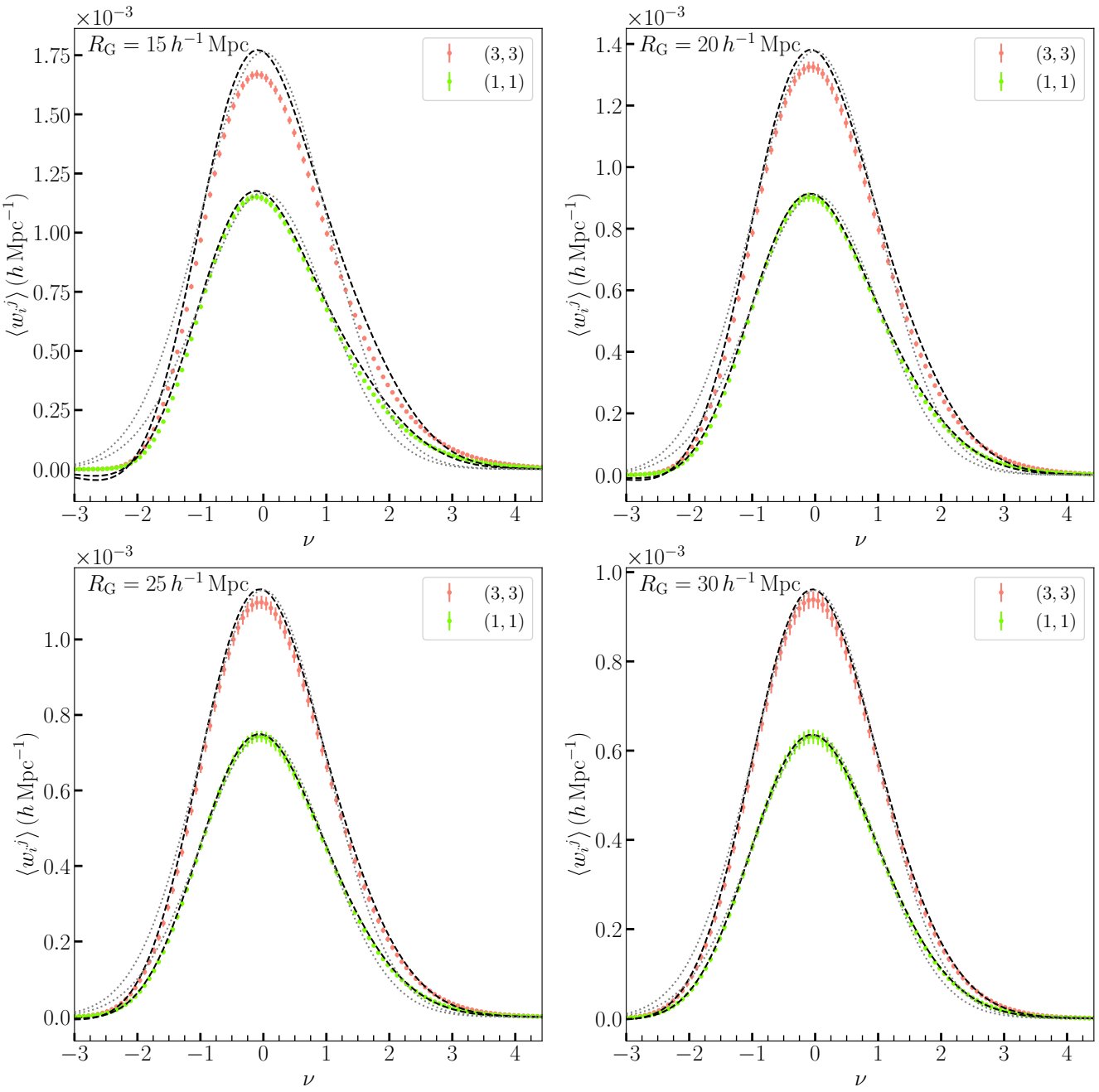

Figure 7. Same as Figure 2, but with zero FOG velocity dispersion, $\sigma_v = \sigma_B = 0$, in the ensemble averages $\langle w_i{}^j \rangle$ and $\langle w_i{}^j \rangle_G$ (black dashed and gray dotted lines, respectively). The discrepancy along the LOS is more significant when contrasted to Figure 2.

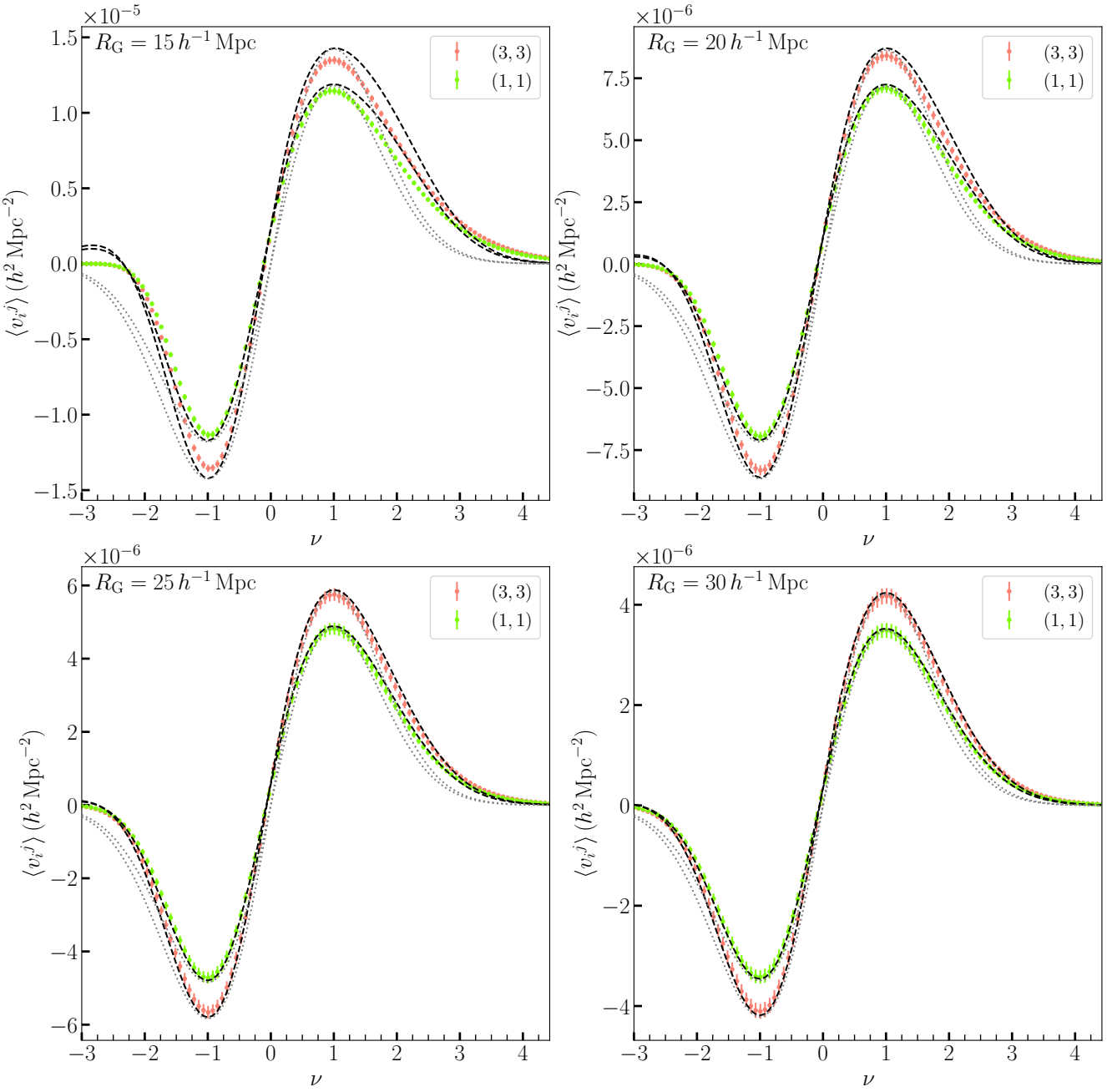

Figure 8. Same as Figure 4, but with zero FOG velocity dispersion, $\sigma_v = \sigma_B = 0$, in the ensemble averages $\langle v_i{}^j \rangle$ and $\langle v_i{}^j \rangle_{\rm G}$ (black dashed and gray dotted lines, respectively). As in Figure 7, the discrepancy along the LOS is more significant when contrasted to Figure 4.

Appendix C
Finite Resolution Effects

In this work we generated discrete dark matter fields on a lattice by binning dark matter particles into a regular grid of resolution $\Delta = 1000/256 = 3.9\,h^{-1}$ Mpc. In this appendix we check that our results are not sensitive to this choice. To do so, we take a small set of $N_{\rm real} = 10$ dark matter particle snapshots at $z = 1$, and bin them into two different resolution grids of $\Delta = 3.9\,h^{-1}$ Mpc and $\Delta = 1000/512 = 1.95\,h^{-1}$ Mpc. The fields are then smoothed using the smallest scale considered in this work, $R_{\rm G} = 15\,h^{-1}$ Mpc and finally we extract the MTs $w_i{}^j$ and $v_i{}^j$. We denote the measured MTs as $\langle w_i{}^j \rangle_{256}$ and $\langle v_i{}^j \rangle_{256}$, and $\langle w_i{}^j \rangle_{512}$ and $\langle v_i{}^j \rangle_{512}$ from the low- and high-resolution fields, respectively.

In the top panels of Figure 9 we present the residuals $\langle w_i{}^j \rangle - \langle w_i{}^j \rangle_G$ and $\langle v_i{}^j \rangle - \langle v_i{}^j \rangle_G$: these are the non-Gaussian signals that we are attempting to measure. These panels are the same as the top left panels of Figures 3 and 5. In these panels we also include the difference between the MTs $\langle w_i{}^j \rangle_{256} - \langle w_i{}^j \rangle_{512}$ and $\langle v_i{}^j \rangle_{256} - \langle v_i{}^j \rangle_{512}$ as black and gray points and error bars, respectively. The points and error bars are, respectively, the mean and error on the mean from the $N_{\rm real} = 10$ realizations and the black and gray points correspond to the (1, 1) and (3, 3) components, respectively. These points are representative of the magnitude of the effect of finite resolution on our results, and are negligible relative to the signal that we are attempting to measure. In the lower panels of the figure

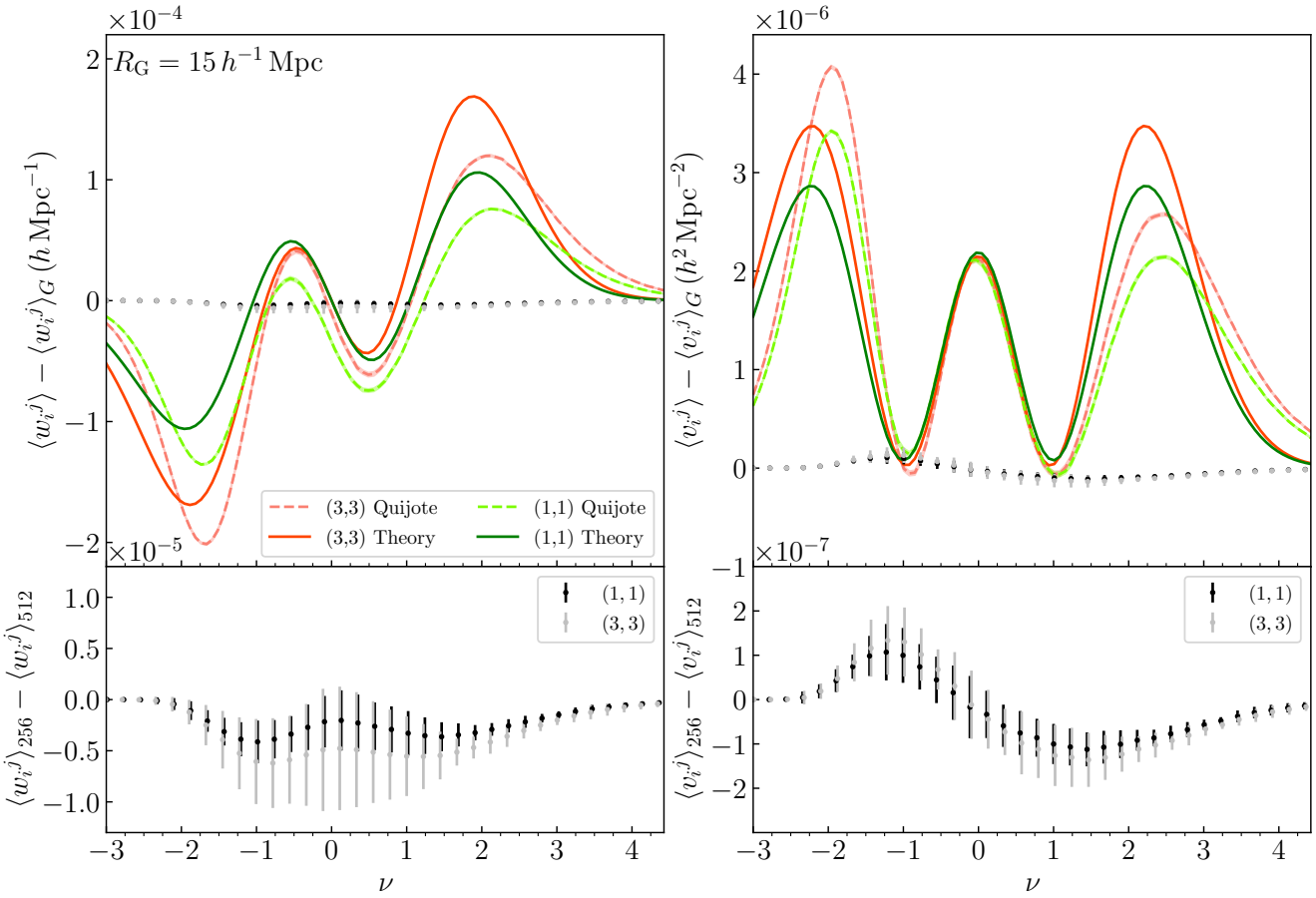

Figure 9. Top panels: the difference between measured values of the MTs ($w_i{}^j$ (left) and $v_i{}^j$ (right)) and their Gaussian expectation values in redshift space, for a field smoothed using $R_G = 15\,h^{-1}$ Mpc. The green and red data are reproduced from the top left panels of Figures 3 and 5, respectively. The black and gray points correspond to the residuals between MTs as measured in high- ($\Delta = 1.95\,h^{-1}$ Mpc) and low-resolution ($\Delta = 3.9\,h^{-1}$ Mpc) fields, respectively. The black and gray points are the (1, 1) and (3, 3) components of the tensors, respectively. Bottom panels: he same black and gray points as in the top panel, but using a smaller y-axis range.

we only plot the $\langle w_i{}^j\rangle_{256} - \langle w_i{}^j\rangle_{512}$ and $\langle v_i{}^j\rangle_{256} - \langle v_i{}^j\rangle_{512}$ residuals using a smaller y-axis range. The lower panels present some nonrandom dependence of the residuals on ν, indicating some systematic effect due to finite resolution, but the effect is an order of magnitude smaller than the non-Gaussian residuals. We note that the effect of finite resolution on the Minkowski functionals has been considered previously, with similar conclusions (C. Park et al. 2005; Y.-R. Kim et al. 2014; S. Appleby et al. 2017).

ORCID iDs

Christophe Pichon https://orcid.org/0000-0003-0695-6735
Pravabati Chingangbam https://orcid.org/0000-0002-7385-8273
Dmitri Pogosyan https://orcid.org/0000-0002-7998-6823
Changbom Park https://orcid.org/0000-0001-9521-6397

References

Abdul-Karim, M., Aguilar, J., Ahlen, S., Alam, S., et al. 2025, PhRvD, 112, 083515
Adler, R. 1981, The Geometry of Random Fields (Wiley)
Afzal, A., Alakhras, M., Kanafi, M. H. J., & Movahed, S. M. S. 2025, MNRAS, 541, 3851
Alesker, S. 1999, Geometriae Dedicata, 74, 241
Appleby, S., Park, C., Hong, S. E., & Kim, J. 2017, ApJ, 836, 45
Appleby, S., Chingangbam, P., Park, C., Yogendran, K. P., & Joby, P. K. 2018, ApJ, 863, 200
Appleby, S., Kochappan, J. P., Chingangbam, P., & Park, C. 2019, ApJ, 887, 128
Appleby, S. A., Park, C., Hong, S. E., Hwang, H. S., & Kim, J. 2020, ApJ, 896, 145
Appleby, S., Park, C., Hong, S. E., et al. 2021, ApJ, 907, 75
Appleby, S., Kochappan, J. P., Chingangbam, P., & Park, C. 2022a, ApJ, 942, 110
Appleby, S., Park, C., Pranav, P., et al. 2022b, ApJ, 928, 108
Ballinger, W. E., Peacock, J. A., & Heavens, A. F. 1996, MNRAS, 282, 877
Bashir, M., Nidharssan, S., Chingangbam, P., et al. 2025, arXiv:2503.17849
Beisbart, C., Buchert, T., & Wagner, H. 2001a, PhyA, 293, 592
Beisbart, C., Valdarnini, R., & Buchert, T. 2001b, A&A, 379, 412
Beisbart, C., Dahlke, R., Mecke, K., & Wagner, H. 2002, LNP, 600, 238
Bernardeau, F., & Pichon, C. 2024, A&A, 689, A105
Bernardo, R. C., Appleby, S., Bernardeau, F., & Pichon, C. 2026, A&A, 705, A18
Beutler, F., Saito, S., Seo, H.-J., et al. 2014, MNRAS, 443, 1065
Bharadwaj, S., Sahni, V., Sathyaprakash, B. S., Shandarin, S. F., & Yess, C. 2000, ApJ, 528, 21
Chingangbam, P., & Park, C. 2013, JCAP, 2013, 031
Chingangbam, P., & Rahman, F. 2024, PhRvD, 109, 083530
Chingangbam, P., Ganesan, V., Yogendran, K. P., & Park, C. 2017a, PhLB, 771, 67
Chingangbam, P., Yogendran, K. P., K., J. P., et al. 2017b, JCAP, 2017, 023
Chingangbam, P., Goyal, P., Yogendran, K. P., & Appleby, S. 2021, PhRvD, 104, 123516
Codis, S., Pichon, C., Pogosyan, D., Bernardeau, F., & Matsubara, T. 2013, MNRAS, 435, 531
Collischon, C., Klatt, M. A., Banday, A. J., Sasaki, M., & Räth, C. 2024, CmPhy, 7, 254

Desjacques, V., & Sheth, R. K. 2010, PhRvD, 81, 023526
Doroshkevich, A. G. 1970, Ap, 6, 320
Feldbrugge, J., van Engelen, M., van de Weygaert, R., Pranav, P., & Vegter, G. 2019, JCAP, 1909, 052
Ganesan, V., & Chingangbam, P. 2017, JCAP, 2017, 023
Gay, C., Pichon, C., & Pogosyan, D. 2012, PhRvD, 85, 023011
Gott, J. R., Dickinson, M., & Melott, A. L. 1986, ApJ, 306, 341
Gott, J. R., Weinberg, D. H., & Melott, A. L. 1987, ApJ, 319, 1
Gott, J. R., III, Park, C., Juszkiewicz, R., et al. 1990, ApJ, 352, 1
Goyal, P., Chingangbam, P., & Appleby, S. 2020, JCAP, 2020, 020
Goyal, P., & Chingangbam, P. 2021, JCAP, 2021, 006
Hadwiger, H. 1957, Vorlesungen über Inhalt, Oberfläche und Isoperimetriee (Grundlehren der mathematischen Wissenschaften) (Springer)
Hamilton, A. J. S. 1998, ASSL, 231, 185
Hamilton, J. S. A., Gott, J. R., & Weinberg, D. 1986, ApJ, 309, 1
Hikage, C., & Matsubara, T. 2012, MNRAS, 425, 2187
Hikage, C., & Yamamoto, K. 2013, JCAP, 2013, 019
Hikage, C., Coles, P., Grossi, M., et al. 2008, MNRAS, 385, 1613
Howlett, C. 2019, MNRAS, 487, 5209
Hug, D., Schneider, R., & Schuster, R. 2008, St. Petersburg Math. J., 19, 137
Joby, P. K., Chingangbam, P., Ghosh, T., Ganesan, V., & Ravikumar, C. D. 2019, JCAP, 1901, 009
Juszkiewicz, R., Fisher, K. B., & Szapudi, I. 1998, ApJL, 504, L1
Kaiser, N. 1987, MNRAS, 227, 1
Kanafi, M. H. J., & Movahed, S. M. S. 2024, ApJ, 963, 31
Kapahtia, A., Chingangbam, P., Appleby, S., & Park, C. 2018, JCAP, 2018, 011
Kapahtia, A., Chingangbam, P., & Appleby, S. 2019, JCAP, 2019, 053
Kapahtia, A., Chingangbam, P., Ghara, R., Appleby, S., & Choudhury, T. R. 2021, JCAP, 2021, 026
Kim, Y.-R., Choi, Y.-Y., Kim, S. S., et al. 2014, ApJS, 212, 22
Kuriki, S., & Matsubara, T. 2023, Advances in Applied Probability, 55, 1390
Liu, W., Jiang, A., & Fang, W. 2022, JCAP, 2022, 045
Liu, W., Jiang, A., & Fang, W. 2023, JCAP, 09, 037
Liu, W., Paillas, E., Cuesta-Lazaro, C., Valogiannis, G., & Fang, W. 2025a, JCAP, 2025, 064
Liu, W., Wu, L., Villaescusa-Navarro, F., et al. 2025b, JCAP, 2025, 088
Marques, G. A., Liu, J., Matilla, J. M. Z., et al. 2019, JCAP, 2019, 019
Matarrese, S., Verde, L., & Heavens, A. F. 1997, MNRAS, 290, 651
Matsubara, T. 1994a, ApJ, 434, L43
Matsubara, T. 1994b, arXiv:astro-ph/9501076
Matsubara, T. 1996, ApJ, 457, 13
Matsubara, T. 2003, ApJ, 584, 1
Matsubara, T. 2024a, PhRvD, 110, 063543
Matsubara, T. 2024b, PhRvD, 110, 063544
Matsubara, T. 2024c, PhRvD, 110, 063545
Matsubara, T. 2024d, PhRvD, 110, 063546
Matsubara, T., & Suto, Y. 1996, ApJ, 460, 51
Matsubara, T., & Yokoyama, J. 1996, ApJ, 463, 409
Matsubara, T., & Kuriki, S. 2021, PhRvD, 104, 103522
Matsubara, T., Hikage, C., & Kuriki, S. 2020, arXiv:2012.00203
McDonald, P. 2011, JCAP, 04, 032
McMullen, P. 1997, Rend. Circ. Palermo, 50, 259
Mecke, K. R., Buchert, T., & Wagner, H. 1994, A&A, 288, 697
Melott, A. L., Weinberg, D. H., & Gott, J. R. 1988, ApJ, 328, 50
Melott, A. L., Cohen, A. P., Hamilton, A. J. S., Gott, J. R., & Weinberg, D. H. 1989, ApJ, 345, 618
Munshi, D., Namikawa, T., McEwen, J. D., Kitching, T. D., & Bouchet, F. R. 2021, MNRAS, 507, 1421
Munshi, D., Smidt, J., Cooray, A., et al. 2013, MNRAS, 434, 2830
Okumura, T., Seljak, U., & Desjacques, V. 2012a, JCAP, 2012, 014
Okumura, T., Seljak, U., McDonald, P., & Desjacques, V. 2012b, JCAP, 2012, 010
Okumura, T., Hand, N., Seljak, U., Vlah, Z., & Desjacques, V. 2015, PhRvD, 92, 103516
Park, C., & Gott, J. R. 1991, ApJ, 378, 457
Park, C., & Kim, Y.-R. 2010, ApJL, 715, L185
Park, C., Gott, J. R., Melott, A. L., & Karachentsev, I. D. 1992, ApJ, 387, 1
Park, C., Vogeley, M. S., Geller, M. J., & Huchra, J. P. 1994, ApJ, 431, 569
Park, C., Gott, J. R., & Choi, Y. J. 2001, ApJ, 553, 33
Park, C., Kim, J., & Gott, J. R. 2005, ApJ, 633, 1
Park, C., Pranav, P., Chingangbam, P., et al. 2013, JKAS, 46, 125
Peacock, J. A., & Dodds, S. J. 1994, MNRAS, 267, 1020
Peebles, P. J. E. 1976, Ap&SS, 45, 3
Pogosyan, D., Gay, C., & Pichon, C. 2009, PhRvD, 80, 081301
Pranav, P., Edelsbrunner, H., van de Weygaert, R., et al. 2017, MNRAS, 465, 4281
Pranav, P., Adler, R. J., Buchert, T., et al. 2019a, A&A, 627, A163
Pranav, P., van de Weygaert, R., Vegter, G., et al. 2019b, MNRAS, 485, 4167
Rahman, F., Chingangbam, P., & Ghosh, T. 2021, JCAP, 2021, 026
Rana, S., Ghosh, T., Bagla, J. S., & Chingangbam, P. 2018, MNRAS, 481, 970
Reid, B. A., & White, M. 2011, MNRAS, 417, 1913
Reid, B. A., Seo, H.-J., Leauthaud, A., Tinker, J. L., & White, M. 2014, MNRAS, 444, 476
Ryden, B. S., Melott, A. L., Craig, D. A., et al. 1989, ApJ, 340, 647
Sahni, V., Sathyaprakash, B. S., & Shandarin, S. F. 1998, ApJL, 495, L5
Saito, S., Baldauf, T., Vlah, Z., et al. 2014, PhRvD, 90, 123522
Santalo, L. A. 1976, Integral Geometry and Geometric Probability (Addison-Wesley Pub. Co), 404
Schmalzing, J., & Buchert, T. 1997, ApJL, 482, L1
Schmalzing, J., & Gorski, K. M. 1998, MNRAS, 297, 355
Schroder-Turk, G., Kapfer, S., Breidenback, B., Beisbart, C., & Mecke, K. 2010, JMic, 238, 57
Schroder-Turk, G. E., Mickel, W., Kapfer, S. C., et al. 2013, NJPh, 15, 083028
Scoccimarro, R. 2004, PhRvD, 70, 083007
Seljak, U., & McDonald, P. 2011, JCAP, 2011, 039
Sellentin, E., Jaffe, A. H., & Heavens, A. F. 2017, arXiv:1709.03452
Shivshankar, N., Pranav, P., Natarajan, V., et al. 2016, ITVCG, 22, 1745
Tinker, J. L. 2007, MNRAS, 374, 477
Tomita, H. 1986, PThPh, 76, 952
Tonegawa, M., Park, C., Zheng, Y., et al. 2020, ApJ, 897, 17
van de Weygaert, R., Pranav, P., Jones, B. J. T., et al. 2011a, arXiv:1110.5528
van de Weygaert, R., Vegter, G., Edelsbrunner, H, et al. 2011b, Trans. Comput. Sci., 14, 60
Villaescusa-Navarro, F., et al. 2020, ApJS, 250, 2
Vlah, Z., Seljak, U., McDonald, P., Okumura, T., & Baldauf, T. 2012, JCAP, 11, 009
Weinberg, D. H., Gott, J. R., & Melott, A. L. 1987, ApJ, 321, 2
Wilding, G., Nevenzeel, K., van de Weygaert, R., et al. 2021, MNRAS, 507, 2968
Yamamoto, M., Becker, M. R., Sheldon, E., Jarvis, M., et al. 2025, MNRAS, 543, 4156
Zunckel, C., Gott, J. R., III, & Lunnan, R. 2011, MNRAS, 412, 1401